Accepted author version of https://doi.org/10.1126/science.adq7280, 6 Dec. 2024

Title: Recent global temperature surge intensified by record-low planetary albedo

Authors: Helge F. Goessling[1*], Thomas Rackow[2], Thomas Jung[1,3]

Affiliations:

[1]Alfred Wegener Institute, Helmholtz Centre for Polar and Marine Research; Bremerhaven, 27570, Germany

[2]European Centre for Medium-Range Weather Forecasts; Bonn, 53175, Germany

[3]Institute of Environmental Physics, University of Bremen; Bremen, 28359, Germany

*Corresponding author. Email: helge.goessling@awi.de

Abstract: In 2023, the global mean temperature soared to almost 1.5K above the pre-industrial level, surpassing the previous record by about 0.17K. Previous best-guess estimates of known drivers including anthropogenic warming and the El Niño onset fall short by about 0.2K in explaining the temperature rise. Utilizing satellite and reanalysis data, we identify a record-low planetary albedo as the primary factor bridging this gap. The decline is apparently caused largely by a reduced low-cloud cover in the northern mid-latitudes and tropics, in continuation of a multi-annual trend. Further exploring the low-cloud trend and understanding how much of it is due to internal variability, reduced aerosol concentrations, or a possibly emerging low-cloud feedback will be crucial for assessing the current and expected future warming.

Main Text:

After the last major El Niño event in 2015/16 global mean warming was offset by a transition to persistent La Niña conditions (*1*; Fig. 2a,b). Since March 2023, however, global sea-surface temperatures have broken records (*2*), well ahead of substantial contributions from the more moderate 2023/24 El Niño (*3*). With the annual global-mean surface temperature (GMST) close to 1.5K above the pre-industrial level, in particular the North Atlantic made headlines with the average surface temperatures exceeding previous records by clear margins (*2*). Concurrently, in 2022/23 the Antarctic sea-ice extent, after decades of a surprising stability (*4*), fell far below previous levels (*5*, *6*).

Besides the onset of El Niño and the expected long-term warming due to anthropogenic greenhouse gases, several factors may have contributed to the anomalous GMST in 2023 (*3*). The 11-year solar cycle is approaching its intensity maximum (*7*); the submarine volcano Hunga Tonga—Hunga Ha'apai (HTHH) has released large amounts of water vapor into the stratosphere, although a net warming effect has been questioned (*8*); and new ship fuel regulations, aimed at reducing sulfur emissions, were implemented in three phases, in 2010, 2015 and 2020 (*9*). While these regulations may be associated with a spatial pattern that is roughly consistent with the pronounced warming of the traffic-heavy North Atlantic and despite further evidence for recent warming due to reduced aerosols (*9, 10, 11, 12*), it has been estimated that the combined global effect of all three factors is below 0.1K (*3)*. This contradicts claims of a much stronger shipping-related effect (*13*) that neglected the delayed response to forcing. An unexplained warming of about 0.2K thus remains (*3)*. Based on CERES-EBAF (hereafter CERES) data (*14, 15, 16; Materials and Methods*), the recent warming has been linked to an unusually large total top-of-atmosphere (TOA) energy imbalance (EEI; *5*).

We use CERES satellite and ERA5 reanalysis (*17, 18; Materials and Methods*) data to explore the causes of the temperature surge. In summary, as synthesized in Fig. 1 and detailed below, we find that the unusually large recent imbalance was mainly driven by a record-low planetary albedo in 2023, continuing a multi-annual trend related to decreasing shortwave reflection by clouds (consistent with *19, 20*). The cloud-related albedo reduction is apparently largely due to a pronounced decline of low-level clouds over the northern mid-latitude and tropical oceans, in particular the Atlantic. The increased absorption of shortwave radiation since December 2020 due to reduced albedo can explain 0.22(±0.04)K of the 2023 temperature anomaly, including 0.030(±0.006)K from polar regions where declining albedo is dominated by sea-ice and snow retreat. Increased incident solar radiation associated with a strong current solar-cycle maximum, captured by CERES but absent in ERA5, has contributed 0.027(±0.005)K to the 2023 temperature anomaly, whereas El Niño has added 0.07(±0.04)K. Disentangling contributions to the low-cloud trend from internal variability, indirect aerosol effects, and a possibly emerging low-cloud feedback remains challenging.

Record-high Earth's energy imbalance and planetary albedo

Earth's energy imbalance (EEI) has been positive for many decades due to increasing greenhouse gas concentrations (*14*). According to CERES, the imbalance has been increasing from 2000 onward (*5, 9, 19, 21*; Fig. 2c), reaching a rate of +0.76$Wm^{-2}dec^{-1}$ during the decade prior to 2023 (Tab. 1). However, a record high was reached in 2023 with an anomaly relative to 2001–2022 of +0.97Wm^{-2}. ERA5 agrees on the positive sign but exhibits lower values, in particular for the imbalance in 2023 (+0.31Wm^{-2}; Tab. 1, Fig. 2c; see *Material and Methods* for a discussion of the uncertainties inherent to ERA5 energy budget diagnostics).

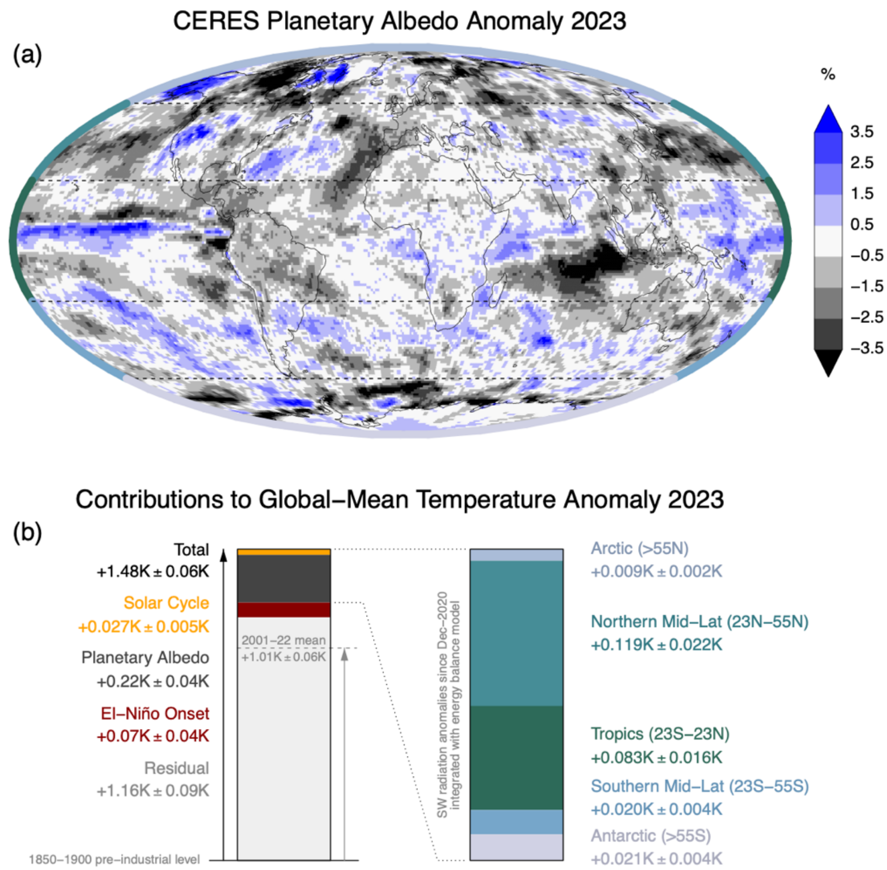

Fig. 1. Synthesis of contributions to Earth's surface temperature anomaly 2023. *(a) CERES planetary albedo anomaly 2023 relative to 2001–2022 (derived from annual-mean TOA incident solar and upwelling solar radiation); (b) contributions to the global-mean surface temperature anomaly 2023 found in this study, with 90% confidence intervals (Materials and Methods), (left) from the El Niño onset (red) and from absorbed solar radiation (ASR) anomalies since December 2020 due to incident solar radiation anomalies (orange) and planetary albedo anomalies (dark gray), and (right) the ASR-related contributions further decomposed into contributions from five zonal bands.*

The EEI trend and 2023 peak are not associated with decreasing outgoing longwave radiation (OLR), as one would expect from increasing greenhouse-gas concentrations in the absence of shortwave feedbacks. Instead, OLR has been increasing and largely offsetting even stronger absorbed solar radiation (ASR) anomalies (*19, 20*; Fig. 2d), consistent with climate models (*22*). The decadal 2013–2022 trend in ASR amounts to $+1.10\text{Wm}^{-2}\text{dec}^{-1}$ in CERES and $+0.97\text{Wm}^{-2}\text{dec}^{-1}$ in ERA5, reaching astonishing anomalies of $+1.82\text{Wm}^{-2}$ in CERES and $+1.31\text{Wm}^{-2}$ in ERA5 in 2023 (Tab. 1, Fig. 2c). Variations of incident solar radiation (ISR), including by the 11-year solar cycle, are an order of magnitude smaller (*3, 7*), implying that reduced planetary albedo is the dominant cause (Figs. 1a,S2b, Tab. 1). It is however striking that, according to CERES, ISR attained a positive anomaly in 2023 of $+0.28\text{Wm}^{-2}$, well above the previous solar-cycle maximum, whereas ERA5 forcing still assumed a negative anomaly of -0.08Wm^{-2} (Fig. S2f, Tab. 1). Given an absolute planetary albedo of about 29% (Fig. S1i), about 0.20Wm^{-2} of the 2023

ASR and imbalance anomalies in CERES can be explained by the ISR peak, and close to half of the discrepancies between CERES and ERA5.

	T *K*	EEI *W/m²*	ASR *W/m²*	CREtc *W/m²*	TC *%*	LC *%*	PA *%*	ISR *W/m²*
CERES Trend 2013–2022 (per decade)	–	+0.76	+1.10	+0.47	-0.37	–	-0.33	-0.01
ERA5 Trend 2013–2022 (per decade)	+0.24	+0.18	+0.97	+1.24	-1.16	-1.27	-0.35	-0.34
CERES Anomaly 2023	– (+0.22)*	+0.97 (-0.44)	+1.82 (+0)	+0.58	-0.34	–	-0.48	+0.28
ERA5 Anomaly 2023	+0.47 (+0.31)	+0.31 (-0.74)	+1.33 (+0)	+1.21	-0.89	-1.51	-0.41	-0.08

Table 1. Decadal trends for 2013–2022 and anomalies for 2023 of selected global-mean quantities related to Earth's temperature, clouds and energy budget. *Trends are per decade and 2023 anomalies are relative to 2001–2022. T = surface (skin) temperature; EEI = Earth's TOA total energy imbalance; ASR = TOA net solar radiation (= absorbed solar radiation); CREtc = TOA solar cloud radiative effect inferred from total cloud cover anomalies; TC = total cloud cover fraction; LC = low-level cloud cover fraction; PA = planetary albedo (derived from global-mean TOA solar downwelling and upwelling radiation); ISR = TOA incident solar radiation. Cyan numbers correspond to counterfactuals based on a 2-layer energy balance model (EBM) where ASR anomalies are assumed to be zero from the beginning of December 2020 onward (as in Figs. 1 and S2). (*derived by combination of the CERES EBM result with the ERA5 temperature anomaly; Materials and Methods)*

Long-term trends in ERA5 can be spurious also due to observing-system changes (*17, 18*). ERA5 however suggests that planetary albedo was possibly relatively low around the 1940's and 50's (Fig. S3i), before industrial aerosol precursor emissions led to global dimming until the 1980's (*23*). The strongest planetary albedo excursions were high-albedo episodes caused by volcanic eruptions, with annual ASR anomalies reaching -3Wm^{-2} in 1992, after the Mount Pinatubo eruption (Fig. S3d). Negative albedo anomalies below the 1950's minimum were however absent. Although uncertain, this suggests that the 2023 planetary albedo may have been the lowest since at least 1940.

Most pronounced changes in the northern hemisphere and tropics

Positive ASR anomalies in 2023 were most pronounced in the northern hemisphere and tropics (Figs. 3b,S4a), consistent with the warming pattern (Fig. 3a). Regional maxima of the 2023 ASR anomaly, locally around 10W/m^{-2}, occurred over the eastern Indian Ocean, over South America and extending over the eastern Pacific in the northern branch of the inter-tropical convergence zone, as well as over northern North America, in the Southern Ocean around 60S, in the subtropical and eastern North Atlantic, and in parts of the North Pacific (Fig. 4d,S6h). All of these are present in both datasets, but the anomalies in the North Atlantic and North Pacific are more pronounced in CERES, which may be related to the handling of aerosols in ERA5 (see below).

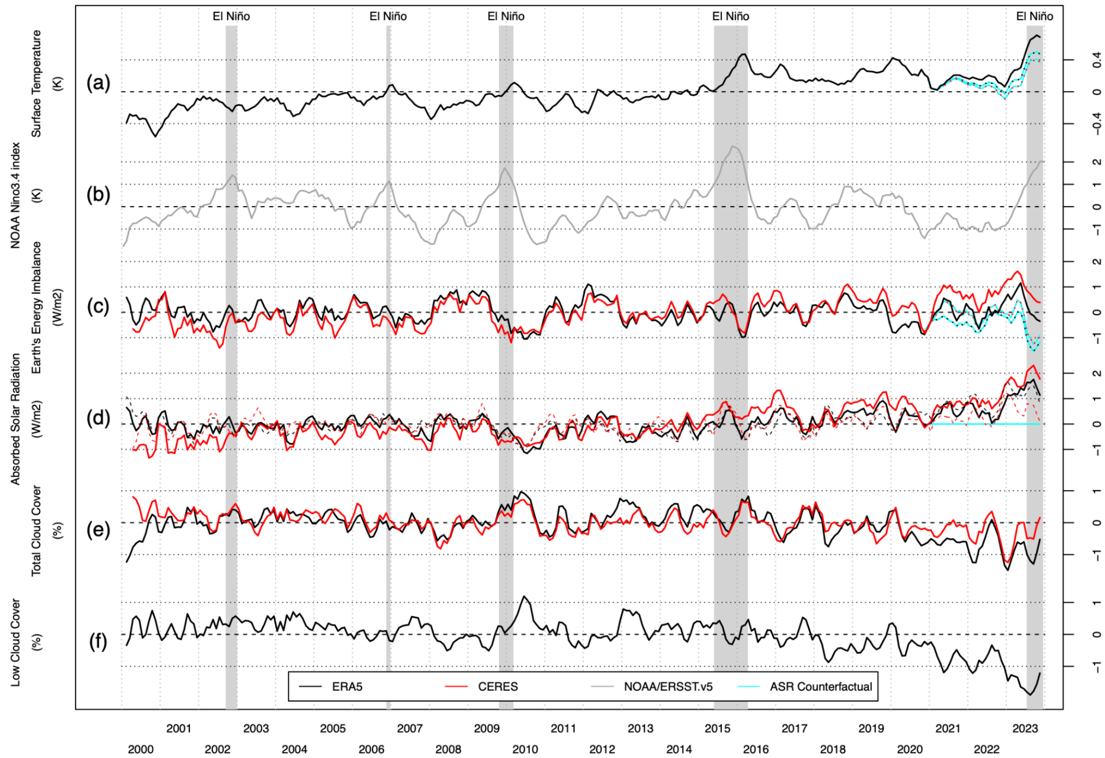

Fig. 2. Global-mean anomalies of key parameters related to Earth's temperature, energy budget and clouds. *Three-month running-mean anomalies relative to 2001–2022 of (a) surface (skin) temperature, (b) NOAA Ocean Niño 3.4 index, (c) Earth's TOA total energy imbalance, (d) TOA net solar radiation (= absorbed solar radiation, ASR), (e) total cloud cover fraction, and (f) low-cloud cover fraction. Red curves show satellite data from CERES and black curves reanalysis data from ERA5. Dashed curves in (d) show the TOA solar cloud radiative effect inferred from total cloud cover anomalies (CREtc). Cyan curves show the full counterfactuals based on a 2-layer energy balance model where ASR anomalies are assumed to be zero from the beginning of December 2020 onward. El Niño periods with anomalies exceeding +1K are highlighted with gray shading. Annual means for ERA5 data starting 1940 and additional quantities are shown in Figs. S1 and S2.*

The positive ASR anomalies over the northern extratropical oceans in 2023 are broadly consistent with decadal trends prior to 2023 (Fig. 4c,d). This is not the case over the tropical Pacific and Indian Ocean, where inter-annual ASR anomalies are dominated by total cloud cover (TCC) changes associated with the El Niño–Southern Oscillation (ENSO; *19, 24, 25, 26, 27*) which transitioned from persistent La Niña to El Niño conditions after 2022 (Fig. 2b). A composite of nine El Niño events based on ERA5 data (*Materials and Methods;* Niño 3.4 index based on *28*) suggests that the albedo signature of El Niño onset years may contribute roughly 5% (+0.08(±0.06)W/m^2 relative to 2001–2022; Fig. S7c) to the total 2023 ASR anomaly. Regionally, ENSO-related cloud and associated ASR patterns (Fig. S7i,j) largely explain inconsistencies between 2023 anomalies and 2013–2022 trends in the tropics (Fig. 4c,d). This includes the strongly positive ASR anomalies (negative cloud anomalies) in the eastern Indian Ocean in 2023.

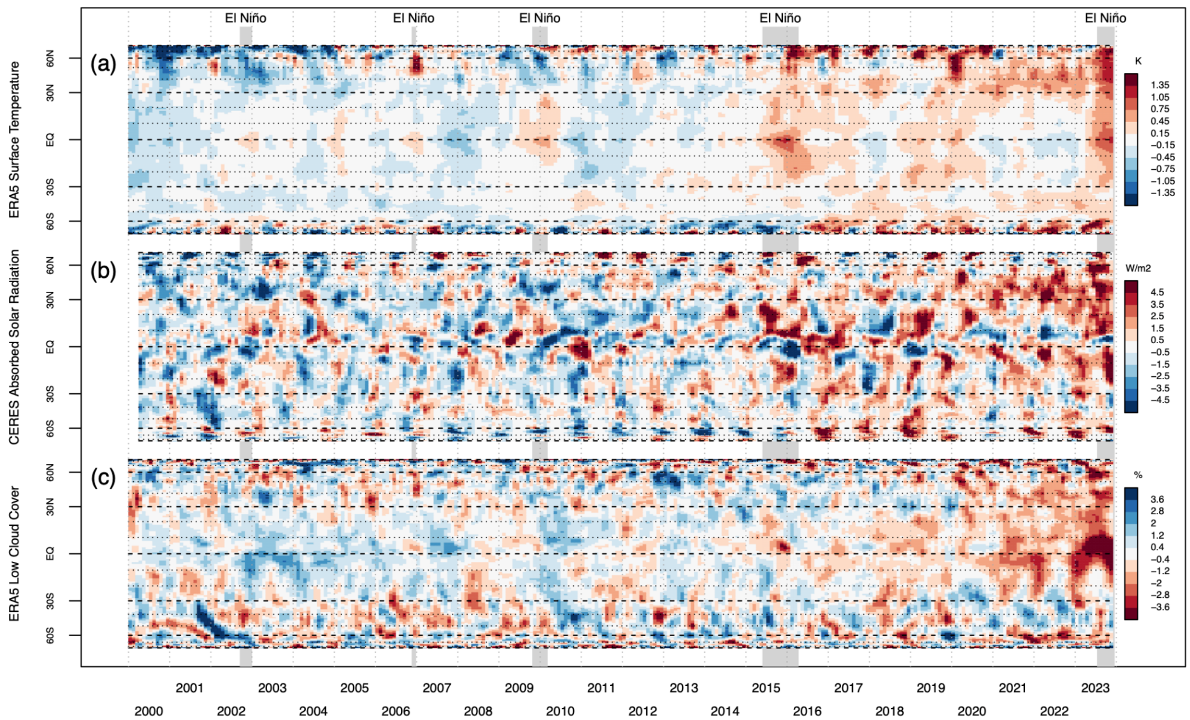

Fig. 3. Zonal-mean anomalies of key parameters related to Earth's temperature, energy budget and clouds. *Three-monthly running-mean anomalies relative to 2001–2022 of (a) ERA5 surface (skin) temperature, (b) CERES absorbed solar radiation, and (c) ERA5 low cloud cover. El Niño periods exceeding +1K are highlighted with gray shading. Latitude spacing corresponds to cosine(latitude) for an equal-area representation. Additional parameters are shown in Fig. S4.*

Before exploring cloud changes more generally, we consider the influence of surface albedo which has been declining since the 1970's (Fig. S3j), first primarily due to Arctic sea-ice and snow retreat (*29*) and since 2016 due to Antarctic sea-ice retreat (*6, 30*). This led to a pronounced seasonal signature in global-mean surface albedo anomalies (Fig. S2c) and polar ASR anomalies (Fig. 3b). In austral summer 2022/23, the surface albedo anomaly of -0.4% was about as strong as the planetary albedo anomaly (Fig. S2b). However, surface albedo anomalies are attenuated by about a factor 3 on average, primarily due to cloud masking (*31, 32*), and even more in the cloudy polar regions (*33*). Surface albedo thus contributed only weakly to the recent planetary albedo decline, in particular when averaged annually and globally, further quantified below.

Absorbed solar radiation anomalies closely linked with cloud changes

Given the central role of clouds in Earth's radiation budget (*19, 21, 24*, *31, 32, 34, 35*), spatial patterns of positive ASR anomalies and trends (Fig. 4c,d) and negative cloud anomalies and trends (Fig. S5a,b) are highly correlated. However, the actual influence of total cloud cover (TCC) on the shortwave cloud radiative effect (CRE) and thus ASR depends strongly on surface albedo and TOA incident solar radiation. To quantify the contribution of changes in TCC and covarying optical depth to ASR anomalies, we have derived empirical relations between TCC and ASR anomalies for CERES and ERA5 based on 2001–2014 data, when ASR was still relatively stationary (*Materials and Methods*).

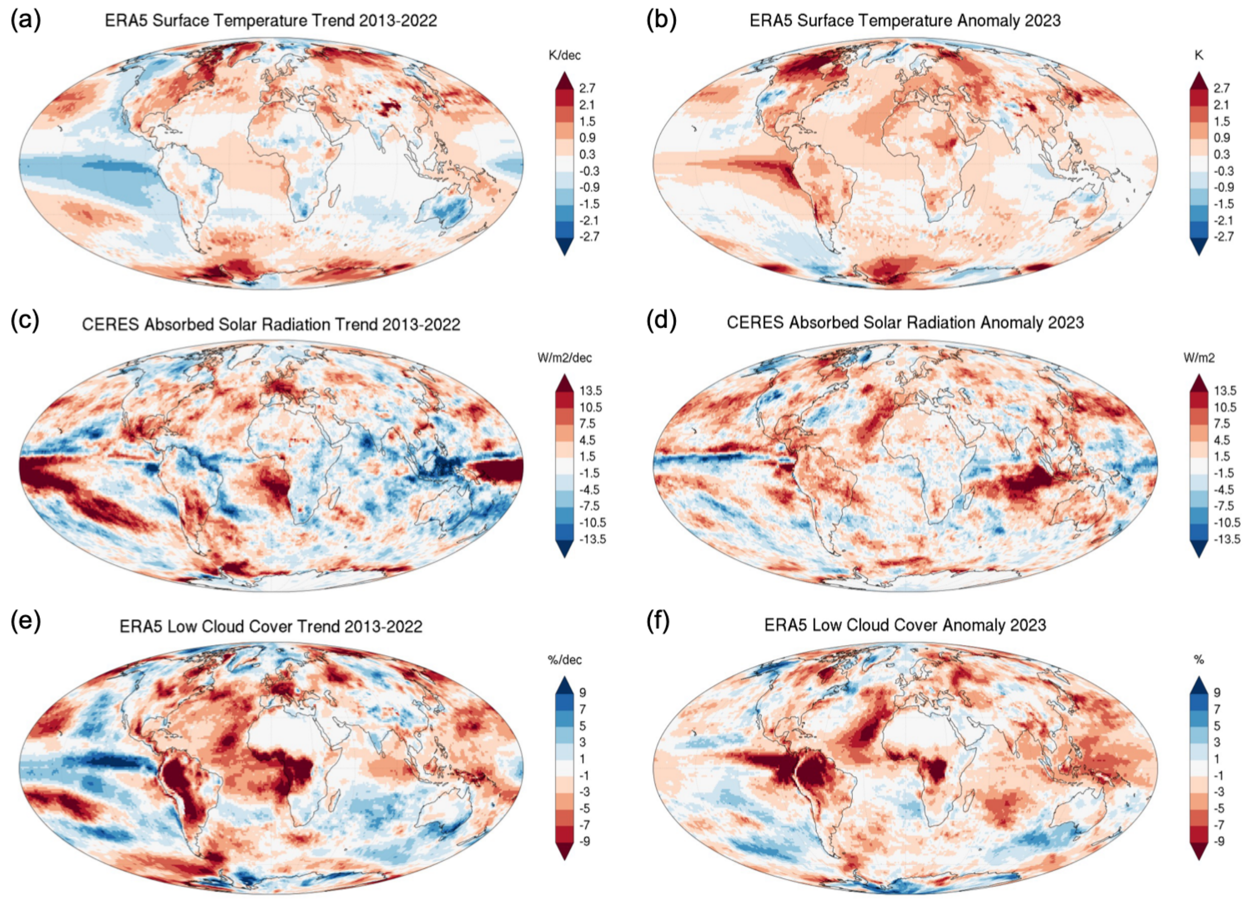

Fig. 4. Decadal 2013–2022 trends and annual-mean 2023 anomalies of key parameters related to Earth's temperature, energy budget and clouds. *Trends and anomalies relative to 2001—2022 of (a,b) ERA5 surface (skin) temperature, (c,d) CERES absorbed solar radiation and (e,f) ERA5 low-cloud cover fraction. Additional parameters are shown in Figs. S5 and S6.*

The shortwave cloud radiative effect inferred from total cloud cover (CREtc) closely resembles spatial ASR patterns (Fig. S5c,d vs. 4c,d), with the exception of the polar regions where surface albedo anomalies linked to sea-ice and snow can dominate ASR anomalies. In ERA5 (Fig. S6c,d vs. S6g,h), not just the patterns but also the magnitudes match closely, with the 2023 global-mean CREtc of $+1.21 W/m^2$ close to the ASR anomaly of $+1.33 W/m^2$ (Tab. 1) and with coherent temporal variations (Fig. 2d). In CERES, however, the CREtc anomalies and trends account for only about one third of the global-mean ASR anomaly and trend (Tab. 1). This is consistent with the combination of a stronger ASR trend in CERES and a weaker total cloud cover trend in CERES compared to ERA5, in particular since 2020 (Fig. 2d,e).

The different degree to which CREtc anomalies contribute to ASR anomalies cannot be explained by different surface albedo contributions, which are similar between the datasets, largely constrained to high latitudes, and overall too small. Rather, it suggests that, according to

CERES, either cloud reflectivity has increased beyond pre-2015 TCC-CRE relations, or clear-sky ASR has increased beyond the influence of surface albedo, or both. Before addressing the possible role of aerosols, which can influence both cloud and clear-sky reflectivity as well as cloud amount (*11, 36*, *37, 38*), we consider the height-dependence of cloud trends.

Cloud anomalies mainly due to reduced low-level clouds

According to ERA5, the total cloud cover trends and anomalies are related mainly to declining low-level cloud cover (LCC; Figs. 2f,3c,4e,f,S3g), whereas high- and mid-level clouds have declined only slightly, if at all (Fig. S2d,e), consistent with *(19)*. Regions with coherent low-cloud reductions both over 2013–2022 and in 2023 include the warm pool region around the Maritime Continent and the northern extratropical western Pacific, as well as large parts of the Atlantic and adjacent land regions. Most of these regions also exhibited reduced total cloud cover (Figs. S5a,b,S6a,b) and thus increased ASR (Figs. 4c,d,S6g,h), with the exception of the eastern warm pool where changes in higher-level clouds have overcompensated the low-cloud reductions.

The South Atlantic between 20°S and the equator did not exhibit negative low-cloud anomalies in 2023, but a pronounced trend prior to 2023. Also in large parts of the East Pacific and South Indian Ocean the 2023 low-cloud anomalies were not consistent with the 2013–2022 trend. This suggests that inter-annual variability has dominated the anomalies and trends there, even though corresponding patterns in the composite of El Niño onset years (Fig. S6e) are weaker.

Globally averaged, the negative low-cloud anomaly in 2023 was about -1.5%, following a decadal trend of -1.27%/decade (Tab. 1). Relative to the absolute global-mean LCC around 38% (Fig. S1j), the 2023 anomaly amounted to astonishing -4.0%. It is striking that the eastern North Atlantic, one of the main drivers of the GMST surge (Fig. 4b; *5*), experienced pronounced low-cloud reductions not only in 2023 (Fig. 4f); almost the entire Atlantic experienced a substantial decline over the previous decade (Fig. 4e).

Further characterizing the cloud anomalies in and beyond 2023 based on more detailed cloud data, such as MODIS-derived cloud properties (*15, 19, 39*), will be important to assess the cloud trends and to further resolve differences between CERES and ERA5. This includes the inconsistent total cloud trends, which may hint at an overestimation of the LCC decline in ERA5 related to the reliance on model physics and unrealistic aerosol handling. More detailed analyses will also be required to understand the causes of the observed cloud and ASR anomalies and trends, including the role of aerosols.

Role of aerosols remains unclear

There is evidence for significant aerosol contributions to recent warming trends (*11*), but isolating the contribution of indirect aerosol effects to cloud amount and reflectivity changes remains challenging. In contrast, the clear-sky absorbed solar radiation (ASR) can provide evidence for direct aerosol effects, despite confounding influences from surface albedo and atmospheric water vapor (*40*). The sea-ice and snow retreat has led to increased global-mean clear-sky ASR (Figs. S2a,S3h) and dominates clear-sky ASR anomalies in high latitudes (Figs. S5e,f,S6e,f). Over the open ocean, however, clear-sky ASR anomalies and trends in CERES (Fig. S5e,f) may hint at direct aerosol effects, albeit these are an order of magnitude smaller compared to the corresponding all-sky values (Fig. 4c,d).

In 2023, CERES clear-sky ASR anomalies were broadly positive between the equator and about 45°N over the Atlantic and Pacific Ocean, with peaks off the East Asian Pacific coast and off the

African Atlantic coast (Fig. S5f). The latter may be related to reduced transport of Saharan dust due to weakened trade winds during northern spring and summer 2023 (*5*), whereas the former and the broader positive signal may hint at reduced aerosols of different origin, possibly due to reduced sulfur emissions from shipping (*9, 41)*. Given that changed aerosol concentrations are a prerequisite for indirect aerosol effects, this also suggests that aerosols may have contributed to the reduced cloud cover and/or cloud reflectivity in these regions (*9, 41)*. However, while the 2013–2022 clear-sky ASR trends suggest a consistent increase along the East Asian Pacific coast, trends prior to 2023 were rather negative over the Atlantic and most of the southern-hemisphere oceans (Fig. S5e). The weak negative incident solar radiation (ISR) trend over this period (Tab. 1) is insufficient to explain these negative clear-sky ASR trends. The contribution of potentially reduced aerosol effects associated with the shipping regulations in 2015 and 2020 thus remains unclear.

Apart from the regions with sea-ice and snow retreat, clear-sky ASR anomalies are much weaker and smoother in ERA5 (Fig. S6e,f) where aerosols are prescribed (*17*) based on forcing data of the Coupled Model Intercomparison Project (CMIP5). Alongside the recent ISR underestimation, this may add to the lower 2023 ASR and imbalance anomalies in ERA5 relative to CERES (Tab. 1), in particular over the North Pacific and North Atlantic.

Temperature response to reduced planetary albedo can explain the warming gap

Earth's climate responds to different types of forcing in a complex way (*42*), but it is possible to estimate the influence of the recent ASR anomalies on GMST with a two-layer energy balance model (EBM; *43, 44*). We construct counterfactuals where ASR anomalies are assumed to be zero from December 2020 onward, about the last time when ASR anomalies were close to zero and when the clearest low-cloud and ASR trends set in (Fig. 2d,f). We integrate monthly CERES and ERA5 ASR anomalies relative to 2001–2022 until December 2023 (*Materials and Methods*; Figs. S10,S11). Subtracting the EBM upper-layer temperature response from the observed GMST provides counterfactual realizations of how GMST may have evolved without the ASR anomalies; counterfactuals of the imbalance (EEI) are constructed in the same way. Additional counterfactuals are constructed with ASR anomalies only from different zonal bands and from incident solar radiation. Considering only the shortwave perturbations is reasonable given that the planetary albedo decline is associated primarily with low-level clouds, which lack the compensating longwave effects of mid- and high-level clouds (*45*).

Based on the full counterfactuals, the 2023 annual-mean GMST may have been 0.25(±0.05)K cooler based on the CERES counterfactual and 0.16(±0.03)K cooler based on the ERA5 counterfactual (cyan curves in Fig. 2a). Subtracting 0.027(±0.005)K due to the solar intensity increase after December 2020 (Fig. S2f) in CERES, not captured in ERA5 (-0.016(±0.003)K), reduces the discrepancy. The full counterfactual total imbalance (EEI) anomaly drops below -1W/m^2 towards the end of 2023 (Fig. 2c). Again adjusting for the solar intensity results in less negative counterfactual EEI anomalies in both cases, more consistent with previous El Niño events. Importantly, the CERES estimate for the effect of planetary albedo alone on the 2023 GMST is +0.22(±0.04)K (Fig. 1b), approximately the magnitude of unexplained warming.

The polar regions beyond 55S and 55N, where surface albedo decline due to sea-ice and snow retreat strongly affects the ASR, jointly contribute +0.030(±0.006)K (12%) to the ASR-driven warming response (Fig. 1b). The remaining 0.19(±0.04)K are dominated by the northern mid-latitudes and tropics where cloud changes drive ASR anomalies. By comparison, based on the Niño 3.4 index in 2023 compared to previous El Niño onset years and their annual-mean GMST anomalies (*Materials and Methods*), El Niño has contributed only +0.07(±0.04)K to the 2023 temperature anomaly. This leaves a residual of +1.16(±0.09)K warming that may have occurred in 2023 without the anomalous ASR and El Niño (Figs. 1b,S8), including the bulk of anthropogenic warming and any additional factors such as longwave effects from the HTHH eruption. The total GMST response of +0.22(±0.04)K to the reduced planetary albedo is broadly consistent with the amount of cooling observed after major volcanic eruptions relative to the respective forcing (Fig. S3a,d; *42, 46*).

Potential implications for climate sensitivity

Three fundamental mechanisms may have contributed to the record-low planetary albedo associated with reduced low-level clouds: internal variability, an emerging low-cloud feedback, and aerosol effects. Contributions from internal variability would subside and leave our expectation of the longer-term warming unaffected. The relative stationarity of the low-cloud cover until about 2015 (Figs. 2f and 3c) speaks against short-term variability, but longer-term variability associated for example with the Atlantic Multidecadal Variability (AMV; *5, 47*) could contribute to the observed trends, also given that ocean surface warming can reduce low-cloud cover (*35, 48, 49*).

The latter mechanism is also essential if the recent trends are due to an emerging low-cloud feedback unrelated to internal variability, complicating a separation of the two. The response of low clouds is the largest source of uncertainty driving differences in climate sensitivity between climate models (*50*). This holds even after the expected range of low-cloud response and climate sensitivity could be reduced with observational constraints (*35, 51*), giving an assessed range of combined marine low-cloud feedback of +0.37(±0.33)W/m^2/K (*51*; *Materials and Methods*). If a substantial low-cloud feedback closer to the upper end of this range now emerges in observations, the lower end of realistic climate sensitivity estimates of 2.3–4.7K (*51*) may need to be adjusted upward.

The average combined shortwave forcing by aerosols in CMIP6 climate models was -1.26W/m^2 (*52*). A near-complete loss of anthropogenic aerosols would thus be required to match the observed ASR anomaly in 2023, speaking either for an underestimated aerosol effect in models (*9*) or strong contributions from internal variability or low-cloud feedback (*19*). Even though the negative correlation between the aerosol effect and climate sensitivity found in CMIP3 (*53*) was weaker in later CMIPs (*52, 54*), a stronger historical aerosol cooling would require a higher sensitivity to greenhouse forcing to reproduce the observed temperature record.

In summary, if the cloud-related albedo decline was caused not solely by internal variability, the 2023 extra heat may be here to stay and Earth's climate sensitivity may be closer to the upper range of current estimates. We may thus be closer to the temperature targets defined in the Paris agreement than previously thought, with potentially strong implications for remaining carbon budgets.

References and Notes

1. T. Iwakiri, Y. Imada, Y. Takaya, T. Kataoka, H. Tatebe, M. Watanabe, Triple-dip La Niña in 2020–23: North Pacific atmosphere drives 2nd year La Niña. *Geophysical Research Letters*, 50, e2023GL105763 (2023). doi:10.1029/2023GL105763

2. Copernicus Climate Change Service (C3S), European State of the Climate 2023, Summary (2024). doi:10.24381/bs9v-8c66
3. G. Schmidt, Climate models can't explain 2023's huge heat anomaly — we could be in uncharted territory. *Nature* **627**, 467 (2024). doi:10.1038/d41586-024-00816-z
4. T. Rackow et al., Delayed Antarctic sea-ice decline in high-resolution climate change simulations. *Nat Commun* **13**, 637 (2022). doi:10.1038/s41467-022-28259-y
5. T. Kuhlbrodt, R. Swaminathan, P. Ceppi, T. Wilder, A Glimpse into the Future: The 2023 Ocean Temperature and Sea Ice Extremes in the Context of Longer-Term Climate Change. *Bull. Amer. Meteor. Soc.* **105**, E474–E485 (2024). doi:10.1175/BAMS-D-23-0209.1
6. L. A. Roach, W. N. Meier, Sea ice in 2023. *Nat Rev Earth Environ* **5**, 235–237 (2024). doi:10.1038/s43017-024-00542-0
7. G. Kopp, Magnitudes and timescales of total solar irradiance variability. *J. Space Weather Space Clim.* **6**, A30 (2016). doi:10.1051/swsc/2016025
8. M. R. Schoeberl et al., Evolution of the climate forcing during the two years after the Hunga Tonga-Hunga Ha'apai eruption. *Journal of Geophysical Research: Atmospheres* **129**, e2024JD041296 (2024). doi:10.1029/2024JD041296
9. J. Hansen et al., Global warming in the pipeline, *Oxford Open Climate Change* **3**, Issue 1, 2023, kgad008 (2024). doi:10.1093/oxfclm/kgad008
10. P. Manshausen, D. Watson-Parris, M. W. Christensen, J. Jalkanen, P. Stier, Invisible ship tracks show large cloud sensitivity to aerosol. *Nature* **610**, 101–106 (2022). doi:10.1038/s41586-022-05122-0
11. Ø. Hodnebrog et al., Recent reductions in aerosol emissions have increased Earth's energy imbalance. *Commun Earth Environ* **5**, 166 (2024). doi:10.1038/s43247-024-01324-8
12. H. Wang et al., Atmosphere teleconnections from abatement of China aerosol emissions exacerbate Northeast Pacific warm blob events. *Proceedings of the National Academy of Sciences* **121(21)**, e2313797121 (2024). doi:10.1073/pnas.2313797121
13. T. Yuan, et al., Abrupt reduction in shipping emission as an inadvertent geoengineering termination shock produces substantial radiative warming. *Commun Earth Environ* **5**, 281 (2024). doi:10.1038/s43247-024-01442-3
14. N. G. Loeb et al., Clouds and the Earth's Radiant Energy System (CERES) Energy Balanced and Filled (EBAF) Top-of-Atmosphere (TOA) Edition-4.0 Data Product. *J. Climate* **31**, 895–918 (2018). doi:10.1175/JCLI-D-17-0208.1
15. P. Minnis P et al., CERES MODIS cloud product retrievals for edition 4—Part I: algorithm changes. *IEEE Trans Geosci Remote Sens* **59**, 2744–2780 (2021). doi:10.1109/TGRS.2020.3008866
16. T. Dudok de Wit, G. Kopp, C. Fröhlich, M. Schöll, Methodology to create a new total solar irradiance record: Making a composite out of multiple data records. *Geophys. Res. Lett.* **44**, 1196–1203 (2017). doi:10.1002/2016GL071866
17. H. Hersbach et al., The ERA5 global reanalysis. *Quarterly Journal of the Royal Meteorological Society* **146(730)**, 1999-2049 (2020). doi:10.1002/qj.3803

18. B. Bell et al., The ERA5 global reanalysis: Preliminary extension to 1950. *Quarterly Journal of the Royal Meteorological Society* **147(741)**, 4186-4227 (2021). doi:10.1002/qj.4174
19. N. G. Loeb et al., Observational Assessment of Changes in Earth's Energy Imbalance Since 2000. *Surv Geophys* (2024). doi:10.1007/s10712-024-09838-8
20. H. Song, Y.-S. Choi, H. Kang, Global change in cloud radiative effect revealed in CERES observations. *Research Square* (2024). Retrieved from https://www.researchsquare.com/article/rs-3781529/v1
21. N. G. Loeb, G. C. Johnson, T. J. Thorsen, J. M. Lyman, F. G. Rose, S. Kato, Satellite and ocean data reveal marked increase in Earth's heating rate. *Geophysical Research Letters* **48**, e2021GL093047 (2021). doi:10.1029/2021GL093047
22. A. Donohoe, K. C. Armour, A. G. Pendergrass, D. S. Battisti, Shortwave and longwave radiative contributions to global warming under increasing CO2. *Proceedings of the National Academy of Sciences* **111(47)**, 16700-16705 (2014). doi:10.1073/pnas.1412190111
23. Y. He, K. Wang, C. Zhou, M. Wild, A revisit of global dimming and brightening based on the sunshine duration. *Geophysical Research Letters* **45**, 4281–4289 (2018). doi:10.1029/2018GL077424
24. S. Kato, Interannual Variability of the Global Radiation Budget. *J. Climate* **22**, 4893–4907 (2009). doi:10.1175/2009JCLI2795.1
25. C. Radley, S. Fueglistaler, L. Donner, Cloud and Radiative Balance Changes in Response to ENSO in Observations and Models. *J. Climate* **27**, 3100–3113 (2014). doi:10.1175/JCLI-D-13-00338.1
26. G. L. Stephens et al., The albedo of Earth. *Rev. Geophys.* **53**, 141–163 (2015). doi: 10.1002/2014RG000449
27. A. Timmermann et al., El Niño–Southern Oscillation complexity. *Nature* **559**, 535–545 (2018). doi:10.1038/s41586-018-0252-6
28. B. Huang et al., Extended Reconstructed Sea Surface Temperature, Version 5 (ERSSTv5): Upgrades, Validations, and Intercomparisons. *J. Climate* **30**, 8179–8205 (2017). doi:10.1175/JCLI-D-16-0836.1.
29. A. Letterly, J. Key, Y. Liu, Arctic climate: changes in sea ice extent outweigh changes in snow cover. *The Cryosphere* **12**, 3373–3382 (2018). doi:10.5194/tc-12-3373-2018
30. A. Riihelä, R. M. Bright, K. Anttila, Recent strengthening of snow and ice albedo feedback driven by Antarctic sea-ice loss. *Nat. Geosci.* **14**, 832–836 (2021). doi:10.1038/s41561-021-00841-x
31. A. Donohoe, D. S. Battisti, Atmospheric and Surface Contributions to Planetary Albedo. *Journal of Climate* **24(16)**, 4402-4418 (2011). doi:10.1175/2011JCLI3946.1
32. N. G. Loeb et al., Decomposing Shortwave Top-of-Atmosphere and Surface Radiative Flux Variations in Terms of Surface and Atmospheric Contributions. *Journal of Climate* **32(16)**, 5003-5019 (2019). doi:10.1175/JCLI-D-18-0826.1
33. S. Kato et al., Seasonal and interannual variations of top-of-atmosphere irradiance and cloud cover over polar regions derived from the CERES data set, *Geophys. Res. Lett.* **33**, L19804 (2006). doi:10.1029/2006GL026685.

34. M. D. Zelinka, S. A. Klein, D. L. Hartmann, Computing and Partitioning Cloud Feedbacks Using Cloud Property Histograms. Part II: Attribution to Changes in Cloud Amount, Altitude, and Optical Depth. *J. Climate* **25(11)**, 3736-3754 (2012). doi:10.1175/JCLI-D-11-00249.1

35. S. A. Klein, A. Hall, J. R. Norris, R. Pincus, Low-cloud feedbacks from cloud-controlling factors: A review. *Surv Geophys* **38**,1307-1329 (2017). doi:10.1007/s10712-017-9433-3

36. S. Twomey, The influence of pollution on the shortwave albedo of clouds. *J. atmos. Sci* **34**, 1149-1152 (1977). doi:10.1175/1520-0469(1977)034<1149:TIOPOT>2.0.CO;2

37. J. Quaas, B. Stevens, P. Stier, U. Lohmann, Interpreting the cloud cover – aerosol optical depth relationship found in satellite data using a general circulation model, *Atmos. Chem. Phys.* **10**, 6129–6135 (2010). doi:10.5194/acp-10-6129-2010

38. J. Li et al., Scattering and absorbing aerosols in the climate system. *Nat Rev Earth Environ* **3**, 363–379 (2022). doi:10.1038/s43017-022-00296-7

39. G. Tselioudis, W. B. Rossow, F. Bender, L. Oreopoulos, J. Remillard, Oceanic cloud trends during the satellite era and their radiative signatures. *Clim Dyn* **62**, 9319–9332 (2024). doi:10.1007/s00382-024-07396-8

40. K. E. Taylor et al., Estimating shortwave radiative forcing and response in climate models. *Journal of Climate*, **20(11)**, 2530-2543 (2007). doi:10.1175/JCLI4143.1

41. M. S. Diamond, Detection of large-scale cloud microphysical changes within a major shipping corridor after implementation of the International Maritime Organization 2020 fuel sulfur regulations, *Atmos. Chem. Phys.* **23**, 8259–8269 (2023). doi:10.5194/acp-23-8259-2023

42. J. Hansen et al., Efficacy of climate forcings, *J. Geophys. Res.* **110**, D18104 (2005). doi:10.1029/2005JD005776

43. I. M. Held et al., Probing the Fast and Slow Components of Global Warming by Returning Abruptly to Preindustrial Forcing. *J. Climate* **23**, 2418–2427 (2010). doi:10.1175/2009JCLI3466.1

44. O. Geoffroy et al., Transient Climate Response in a Two-Layer Energy-Balance Model. Part I: Analytical Solution and Parameter Calibration Using CMIP5 AOGCM Experiments. *J. Climate* **26**, 1841–1857 (2013). doi:10.1175/JCLI-D-12-00195.1

45. M. D. Zelinka, C. Zhou, S. A. Klein, Insights from a refined decomposition of cloud feedbacks. *Geophys. Res. Lett.* **43**, 9259–9269 (2016). doi:10.1002/2016GL069917

46. D. Zanchettin et al., Effects of forcing differences and initial conditions on inter-model agreement in the VolMIP volc-pinatubo-full experiment. *Geosci. Model Dev.* **15**, 2265–2292 (2022). doi:10.5194/gmd-15-2265-2022

47. K. Li, F. Zheng, J. Zhu, Q.-C. Zeng, El Niño and the AMO Sparked the Astonishingly Large Margin of Warming in the Global Mean Surface Temperature in 2023. *Adv. Atmos. Sci.* **41**, 1017-1022 (2024). doi:10.1007/s00376-023-3371-4

48. C. L. Boehm, D. W. J. Thompson, The Key Role of Cloud–Climate Coupling in Extratropical Sea Surface Temperature Variability. *J. Climate* **36**, 2753–2762 (2023), doi:10.1175/JCLI-D-22-0362.1

49. M. Athanase, A. Sánchez-Benítez, H. F. Goessling, F. Pithan, T. Jung, Projected amplification of summer marine heatwaves in a warming Northeast Pacific Ocean. *Commun Earth Environ* **5**, 53 (2024). doi:10.1038/s43247-024-01212-1

50. X. Qu, A. Hall, S. A. Klein, P. M. Caldwell, On the spread of changes in marine low cloud cover in climate model simulations of the 21st century. *Clim Dyn* **42**, 2603–2626 (2014), doi:10.1007/s00382-013-1945-z

51. S. C. Sherwood et al., An assessment of Earth's climate sensitivity using multiple lines of evidence. *Reviews of Geophysics* **58**, e2019RG000678 (2020). doi:10.1029/2019RG000678

52. C. J. Smith et al., Effective radiative forcing and adjustments in CMIP6 models. *Atmos. Chem. Phys.* **20**, 9591–9618 (2020). doi:10.5194/acp-20-9591-2020

53. J. T. Kiehl, Twentieth century climate model response and climate sensitivity. *Geophys. Res. Lett.* **34**, L22710 (2007). doi:10.1029/2007GL031383

54. P. M. Forster et al., Evaluating adjusted forcing and model spread for historical and future scenarios in the CMIP5 generation of climate models. *J. Geophys. Res. Atmos.* **118**, 1139–1150 (2013). doi:10.1002/jgrd.50174

Acknowledgments: We thank Hans Hersbach and Adrian Simmons for answering our questions about the interpretation of ERA5 trends and aerosol handling. Sebastian Bathiany, Tobias Becker, Suvarchal Cheedela and Antje Boetius provided very valuable comments on a draft version of this paper. We are grateful to the Copernicus Climate Change Service (C3S) and the National Aeronautics and Space Administration (NASA) for the development, production and provision of the invaluable CERES-EBAF and ERA5 data sets. We thank the German Climate Computing Centre (DKRZ) for providing simple access to the ERA5 data and computing resources for the data analysis. We also thank the two anonymous reviewers for thoughtful remarks that helped improve this work.

Funding: HFG and TJ based on internal funds of the Alfred Wegener Institute, Helmholtz Centre for Polar and Marine Research, which is part of the Helmholtz Association and funded by the Germany Ministry of Education and Research (BMBF). This research has been supported by the European Commission Horizon 2020 Framework Programme nextGEMS (grant no. 101003470).

Author contributions: Conceptualization: HFG; Methodology: HFG, TR; Investigation: HFG, TR, TJ; Visualization: HFG, TR; Funding acquisition: /; Project administration: /; Supervision: /; Writing – original draft: HFG, TR, TJ; Writing – review & editing: HFG, TR, TJ

Competing interests: Authors declare that they have no competing interests.

Data and materials availability: ERA5 data is available from the Copernicus Climate Change Service (C3S) Climate Data Storage at https://cds.climate.copernicus.eu/. CERES-EBAF data is available from NASA at https://asdc.larc.nasa.gov/project/CERES. NOAA Climate Prediction Center Ocean Niño Index data is available at https://www.cpc.ncep.noaa.gov/data/indices/oni.ascii.txt.

Supplementary Materials

Materials and Methods

Data

Temperature, cloud and albedo signatures of El Niño

Empirical estimation of total cloud cover-inferred ASR anomalies

2-layer energy balance model and ASR-based counterfactuals

Uncertainty estimation

Figs. S1 to S11

Table S1

Supplementary Materials for

Recent global temperature surge intensified by record-low planetary albedo

Helge F. Goessling, Thomas Rackow, and Thomas Jung

Corresponding author: helge.goessling@awi.de

The PDF file includes:

Materials and Methods

Data

We use three public datasets to explore Earth's energy budget, surface temperature and clouds, namely (i) the Clouds and the Earth's Radiant Energy System (CERES) Energy Balanced and Filled (EBAF) Top-of-Atmosphere (TOA) Edition-4.2 Data Product from the US National Aeronautics and Space Administration (NASA; *14*, hereafter CERES), (ii) the ERA5 reanalysis produced by the European Centre for Medium-Range Weather Forecasts (ECMWF; *17, 18*), and the Ocean Niño 3.4 Index (ONI) produced by the US National Oceanic and Atmospheric Administration (NOAA).

CERES is a satellite-based product intended to provide a long-term record for detecting decadal changes in Earth's global radiation budget, clouds and aerosols (*14*). Besides measurements of radiation emitted from Earth, the CERES-EBAF product also includes measurements of TOA incident solar radiation based on a composite out of multiple data records (*16*). CERES includes a one-time adjustment of the TOA fluxes to ensure that the global-mean net TOA flux for July 2005–June 2015 is consistent with an in-situ value of 0.71 Wm^{-2}. In addition to the monthly TOA all-sky and clear-sky radiation fluxes on a 1-degree longitude-latitude grid, available from March 2000–December 2023, we use the total cloud cover fractions based on the Moderate Resolution Imaging Spectrometer (MODIS) contained in the CERES product (*15*).

ERA5 is ECMWF's latest reanalysis product, updated on a daily basis in near-real-time (*17, 18*). It combines an extensive set of satellite and in-situ observational data with a fixed version of ECMWF's physical numerical weather prediction model by a sophisticated data assimilation scheme. It thereby provides a gap-free global gridded estimate of the evolution of a large number of variables, including clouds and radiation fluxes, reaching back to January 1940. Long-term trends in ERA5 need to be interpreted with caution due to possible shifts resulting from changes in the observing system, including strongly reduced data density in earlier decades. Moreover, due to the data assimilation, total mass and energy budgets in ERA5 are not closed (17). This implies that absolute values of quantities like the top-of-atmosphere total imbalance (EEI) are spurious. It is thus important to consider anomalies, like we do throughout this work, rather than absolute values.

Given that CERES data is also subject to uncertainties, we use ERA5 (i) as an additional data product, even though not fully independent as the satellite data sources are overlapping, (ii) to get some evidence for the evolution of relevant parameters before March 2000, keeping in mind the possibility of spurious trends, and (iii) to analyze the height-dependence of cloud changes based on three categories, namely low-level (atmospheric pressure above about 800hPa), mid-level (atmospheric pressure between about 800hPa and 450hPa), and high-level (atmospheric pressure below about 450hPa) clouds. For consistency, all monthly ERA5 data has been remapped from the original 0.28-degree grid to the 1-degree CERES grid by first-order conservative remapping prior to analysis.

Total cloud cover is about 4-5% lower in ERA5, although this may be due to differences in cloud definitions rather than being an actual bias. Apart from that, global-mean ERA5 and CERES climatologies are matching rather closely (Fig. S1). Generally, spatio-temporal variations are consistent between the datasets, as visible in numerous figures in this study, suggesting that ERA5 is suitable for the purposes listed above. A notable exception is the TOA incident solar radiation (ISR) where the forcing data in ERA5 starts to diverge from the observation-based CERES values in 2020. The reason is that ERA5 ISR is based on reconstructed/observed data only until 2008 and assumes a perpetual repetition of the last solar cycle thereafter (*17*). Similarly, sulfate aerosols in ERA5 follow CMIP5 historical and scenario forcings, although based on historical emission estimates until 2009 and scenario data thereafter (*17*).

The NOAA Niño 3.4 index is constructed from 3-month running means of ERSST.v5 sea-surface temperature anomalies in the Niño 3.4 region (5S–5N, 170W–120W), based on centered 30-year base periods updated every 5 years (*28*).

Temperature, cloud and albedo signatures of El Niño

El Niño is a key driver of inter-annual climate variability (*25, 27*). Given that conditions in 2023 transitioned from La Niña to El Niño (Fig. 2b), we estimate the impact of El Niño on temperatures, radiation fluxes and clouds in 2023 based on previous El Niño events. We consider a set of the 4 pre-2023 El Niño events covered by the CERES period (2002/03, 2006/07, 2009/10, 2015/16) based on CERES and ERA5 data, and an extended set of 9 pre-2023 El Niño events (1951/52, 1957/58, 1968/69, 1972/73, 1997/98, 2002/03, 2006/07, 2009/10, 2015/16) based on ERA5 data. Events influenced by volcanic eruptions and the double-event 1987/88 (Fig. S3) are excluded. To isolate anomalies associated only with El Niño, anomalies for each event have been normalized by subtracting the average anomalies of the two years flanking each event, that is, the year before the El Niño onset year and the year after the El Niño second year. Nonlinear longer-term trends, including seasonally-varying ones, are thereby removed. We consider multi-event composites to estimate the temporal evolution of several parameters over the course of an average event (Fig. S7), including the shortwave signature, and individual events to estimate the temperature anomaly due to El-Niño in 2023 (Fig. S8). Given that 2023 was an El Niño onset year, the main focus is on these.

During El Niño, warmer ocean surface waters are exposed in the eastern tropical Pacific by internal redistribution of water masses (*27*; Fig. S7g), resulting in higher global-mean surface temperature (Figs. 2a,b,S7a). During previous events, the normalized annual-mean GMST anomaly during El Niño onset years was mostly around +0.05K to +0.10K, with a dependence on the annual-mean Niño 3.4 index (Fig. S8). Based on the 2023-mean Niño 3.4 index anomaly and linear least-squares regression, we estimate that El Niño has contributed about +0.07(±0.04)K (90% confidence interval) to the 2023 temperature anomaly.

Modulated by a complex interplay of different energy fluxes and mechanisms, the surface warming associated with El Niño leads to increased global-mean TOA outgoing longwave radiation. This results in a decreased total imbalance (EEI) (Fig. S7b, consistent with *25*), although modified by a total absorbed solar radiation (ASR) signature (Fig. S7c,h) and hence a planetary albedo signature (Fig. S7d) related mainly to cloud patterns (Fig. S7e,f,i,j) (*24*, *25*, *26*). Based on the ERA5-based nine-event composite, the global and annual-mean ASR signature during El Niño onset years is +0.08(±0.06)Wm^{-2} (planetary albedo about -0.02%; dashed curves in Fig. S7c,d) and thus only a small fraction of the total 2023 ASR anomaly of +1.82Wm^{-2} in CERES and +1.33Wm^{-2} in ERA5. The contribution of the El Niño albedo signature to the 2023 GMST anomaly is about an order of magnitude smaller compared to the general temperature signature of +0.07(±0.04)K (see above). The possible ASR contribution of El Niño is thus not treated separately in counterfactuals based on the energy balance model integrations (see below).

Empirical estimation of total cloud cover-inferred ASR anomalies

To estimate the contribution of total cloud cover (TCC) changes to the ASR anomalies and trends, we have fitted power functions of the form

(1) $CRE = \alpha \cdot TCC^{\beta}$

to the monthly-mean TCC and shortwave cloud radiative effect (CRE) data for each of the 1-degree grid points for each calendar month and dataset separately. To keep the parameters within physically reasonable bounds even where the TOA incident solar radiation is very small or CRE variations are strongly confounded by surface albedo variations, we bounded α within [-ISR,ISR] and β within [1,4]. We have used only the inter-annual variations within 2001–2014, because during this period global-mean ASR and low-cloud cover were still relatively stationary (Fig. 2d,f) and in order to exclude any potential aerosol-cloud effects that might have been caused by the two IMO regulation changes in 2015 and 2020. Given the small sample size, for each grid point we have also included the data of neighboring grid cells within 2 degrees in meridional and zonal direction, as long as the climatological surface albedo differs by at most 5%.

Results of fitted parameters and explained variance are shown exemplarily for May in Fig. S9. The fitted power functions have subsequently been used to infer a hypothetical CRE going back to TCC-anomalies alone, termed CREtc (Figs. 2d,S1f,S4b,d,S5c,d,S6c,d, Tab. 1). CREtc accounts not only for an isolated cloud amount effect, where CRE is proportional to TCC (*34*), but also for changes in CRE through covariances between TCC and cloud optical depth and altitude. We find that, arguably due to these covariances, cloud radiative effect typically depends superlinearly on total cloud cover in both datasets (Fig. S9c,d), with regional differences that may be related to the dependence of cloud overlap on cloud regimes.

2-layer energy balance model and ASR-based counterfactuals

The 2-layer energy balance model (EBM) used in this study to estimate temperature responses to absorbed solar radiation (ASR) anomalies follows earlier work by (*43*) and (*44*). The EBM adopted here splits the Earth system into two main layers. It describes the evolution of upper-layer temperature perturbations T and a deep-ocean layer temperature perturbation T_0 over time as a system of two ordinary differential equations (ODEs)

(2) $C\frac{dT(t)}{dt} = F(t) - \lambda T(t) - \gamma(T(t) - T_0(t))$

(3) $C_0\frac{dT_0(t)}{dt} = \gamma(T(t) - T_0(t))$,

where C is a heat capacity for the atmosphere-land-upper-ocean system; F is a radiative forcing amplitude function that may vary over time, t; λ is the radiative feedback parameter for a CO_2 perturbation; γ is an exchange coefficient between the upper and deeper ocean layers; and C_0 is the deep-ocean heat capacity. The parameters of the EBM follow Tables 3 and 4 in (*44*), where parameter fits to CMIP5 models are presented. For our central estimates we use the CMIP5 multi-model mean (MMM, based on 15 models) for the individual parameters, as repeated for convenience in Table S1. In addition, we use the sets of parameters corresponding to each of the CMIP5 models individually to derive uncertainties for the estimated temperature response contributions (see next section). Solar forcing is less effective than an equivalent CO_2 forcing, with an efficacy of $F_{eff} = 92\%$ (*42*). Originally this estimate is for ASR anomalies due to solar intensity anomalies rather than planetary albedo anomalies, but we assume that it holds for the latter, too. We thus multiply by this factor in F when using ASR anomalies from ERA5 or CERES as input to the EBM.

Another way to look at the system of equations is that the left-hand sides of the ODEs describe the tendencies of upper-layer (Eq. 2) and deep-layer (Eq. 3) heat contents (*44*). The chosen MMM value for the upper-layer C heat content roughly implies an effective mixed layer thickness of 77m (*44*). With the chosen mean values, the upper and deeper ocean layers respond on a timescale of 4.1 years and 219 years, respectively (*44*).

The 2-layer EBM has simple analytical solutions for linear and step-wise forcing functions F (*44*). In our implementation, the system of ODEs is solved numerically with a Forward Euler discretisation and monthly timesteps. For a simple step-wise forcing, our numerical solution agrees with the analytical solutions given by (*44*). The EBM returns monthly T, T_0, and Earth Energy Imbalance (EEI), $F - \lambda T$, as output.

To construct ASR-based counterfactuals where ASR anomalies are assumed to be zero from some time onward, we drive the EBM with monthly CERES and ERA5 ASR anomalies relative to 2001–2022 until December 2023, starting in December each year from 2001 to 2022 (Figs. S10,S11). Subtracting the EBM upper-layer temperature response from the observed GMST provides counterfactuals of how GMST may have evolved without the ASR anomalies. Counterfactuals of the imbalance (EEI) are constructed in the same way. Considering only the shortwave perturbations is reasonable given that the planetary albedo decline is associated primarily with low-level clouds, which lack the compensating longwave effects of mid- and high-level clouds (*45*). We focus on the counterfactuals starting December 2020 because that was about the last time when ASR anomalies in satellite data were close to zero and when the clearest low-cloud and ASR trends set in (Fig. 2d,f).

Additional counterfactuals are constructed by separately using the contributions to the global-mean ASR anomalies (i) from five different zonal bands (Antarctic 90S–55S; Southern mid-latitudes 55S–23S; Tropics 23S–23N; Northern mid-latitudes 23N–55N; Arctic 55N–90N) and (ii) from anomalies of the TOA incident solar radiation (Fig. S2f) by multiplication with the spatio-temporal pattern of absolute planetary albedo. Case (i) also serves to approximate the contribution of surface albedo trends to the global planetary albedo trend. This is reasonable because, first, surface albedo trends are dominated by sea-ice and snow retreat poleward of 55S and 55N and, second, surface albedo trends dominate total planetary albedo trends there.

Uncertainty estimation

All uncertainty estimates provided in this study correspond to 90% confidence intervals. The exact methods and assumptions necessarily differ for different estimates as follows.

The 2023 GMST increase above pre-industrial, referred to as "almost 1.5K" and "close to 1.5K" in the abstract and main text, is relative to 1850—1900, following the C3S and WMO standard based on IPCC AR5 and AR6 (*2*). The uncertainty of the contemporary warming is primarily related to the uncertainty associated with the pre-industrial level, which is about ±0.06K (width of 90% confidence interval) according to C3S (*2*). GMST warming estimates for 2023 from different datasets, provided by C3S (*2*), are: 1.483K (ERA5), 1.468K (JRA-3Q), 1.446K (Berkeley Earth), 1.436K (GISTEMP), 1.438K (HadCRUT5), and 1.443K (NOAAGlobalTemp). In Fig. 1 and for the computation of the uncertainty associated with the "residual warming" (see below) we use the (rounded) ERA5 estimate of +1.48(±0.06)K, including the broader uncertainty estimate from C3S (*2*). Regarding the question by how much the 2023 GMST was above the previous annual record, which was 2016 according to all datasets, the range of estimates is: 0.168K (ERA5), 0.152K (JRA-3Q), 0.167K (Berkeley Earth), 0.152K (GISTEMP), 0.170K (HadCRUT5), and 0.158K (NOAAGlobalTemp). For consistency, in the abstract we refer to the (rounded) ERA5 estimate of "about 0.17K".

For the ASR signature of the El-Niño onset (+0.08(±0.06)W/m^2), the half-width of the 90% confidence interval is based on the standard error of the annual-mean ASR of the nine previous El-Niño onset years contributing to the composite, individually normalized as described above. The standard error is multiplied by the 95% quantile of a normal distribution with zero mean and unit standard deviation (≈1.645).

The confidence interval for the GMST anomaly associated with El Niño onset years (+0.07(±0.04)K), derived from the nine previous El Niño onset years (Fig. S8), is the 90% confidence interval of the linear least-squares regression used to predict the annual-mean GMST anomaly from the annual-mean Niño 3.4 index.

A central outcome of this study are the estimates for the 2023 annual-mean GMST response to the various components of the ASR anomalies since December 2020 (see most of the estimates shown in Fig. 1b). For these, the CERES ASR anomalies are considered to be more reliable given the limitations of the ERA5 data outlined above, although the ERA5-based estimates may be regarded as a qualitative indicator of reliability/uncertainty. Like any real-world measurements, also the CERES-based ASR anomalies come with uncertainties, but an accurate quantification of these is beyond the scope of this study. Instead, we have quantified the uncertainty associated with the EBM-based derivation of the 2023 annual-mean GMST response from the ASR anomalies. To this end we have constructed an ensemble of EBMs using parameters fitted to each of the CMIP5 models analyzed in (*44*). Feeding the same

ASR anomalies into each of the EBM variants provides an ensemble of GMST responses. 90% confidence intervals are obtained by multiplying the ensemble standard deviation of the 2023 annual-mean GMST response by the 95% quantile of a normal distribution with zero mean and unit standard deviation (≈1.645).

The uncertainty estimates for the GMST response to ASR anomalies thus reflect the model-based uncertainties of Earth's climate sensitivity and response timescales but do not account for uncertainties associated with the ASR anomalies. We however note that, when removing the global ASR difference between CERES and ERA5 due to the ISR offset to derive the purely albedo-related GMST response, the 90% confidence intervals derived from CERES (+0.22(±0.04)K) versus ERA5 (+0.18(±0.03)K) are consistent. Additional uncertainties arise from the choices made regarding the start date of the ASR-based counterfactuals (December 2020; compare other start dates in Figs. S10,11) and the baseline for the anomalies (2001—2022). These choices were made due to the apparent onset of clear ASR and cloud-cover anomalies around December 2020 and in order to maximize the sample size of the baseline without including the exceptional year of 2023. Still, the GMST response estimates must be regarded as conditional on these choices.

The estimates for the combined marine low-cloud feedback of +0.37(±0.33)W/m^2/K and the equilibrium climate sensitivity of 2.3–4.7K correspond to 90% confidence ranges based on (*51*). The latter is taken from (*51*) directly, whereas the low-cloud feedback is the sum of the "Tropical marine low cloud" and the "Middle-latitude marine low-cloud amount" terms (their Tab. 1), with the uncertainty derived by Gaussian error propagation and multiplication by the 95% quantile of a normal distribution with zero mean and unit standard deviation (≈1.645).

Finally, no estimates of statistical significance are provided for the decadal trends shown in this study (Tab. 1, Figs. 4,S5,S6) for the following reasons. It is practically impossible to derive statistical significance of decadal trends in an unambiguous way for climate-related variables given an unknown degree of internal variability across timescales, including multi-decadal. This is already the case for global-mean trends, but even more so for local trends given lower signal-to-noise ratios. For example, decadal trends are strongly influenced by ENSO, as discussed in this study. The problems posed by unknown internal variability cannot be addressed properly by simply taking into account annual-scale autocorrelation when testing for significance of trends, and estimates for annual-scale autocorrelations are highly uncertain given that the CERES data extends over not even 25 years. An additional issue are the uncertainties associated with forced changes, including their temporal nonlinearity. For these reasons we can use the decadal trends reported here only for qualitative evidence, to explore whether the anomalies observed in 2023 may be part of emerging trends. Consistently with this rather qualitative approach aimed at plausibility, we leave the question largely unanswered how much of the trends and anomalies are linked to forced changes (be it with or without feedbacks involved) versus internal variability.

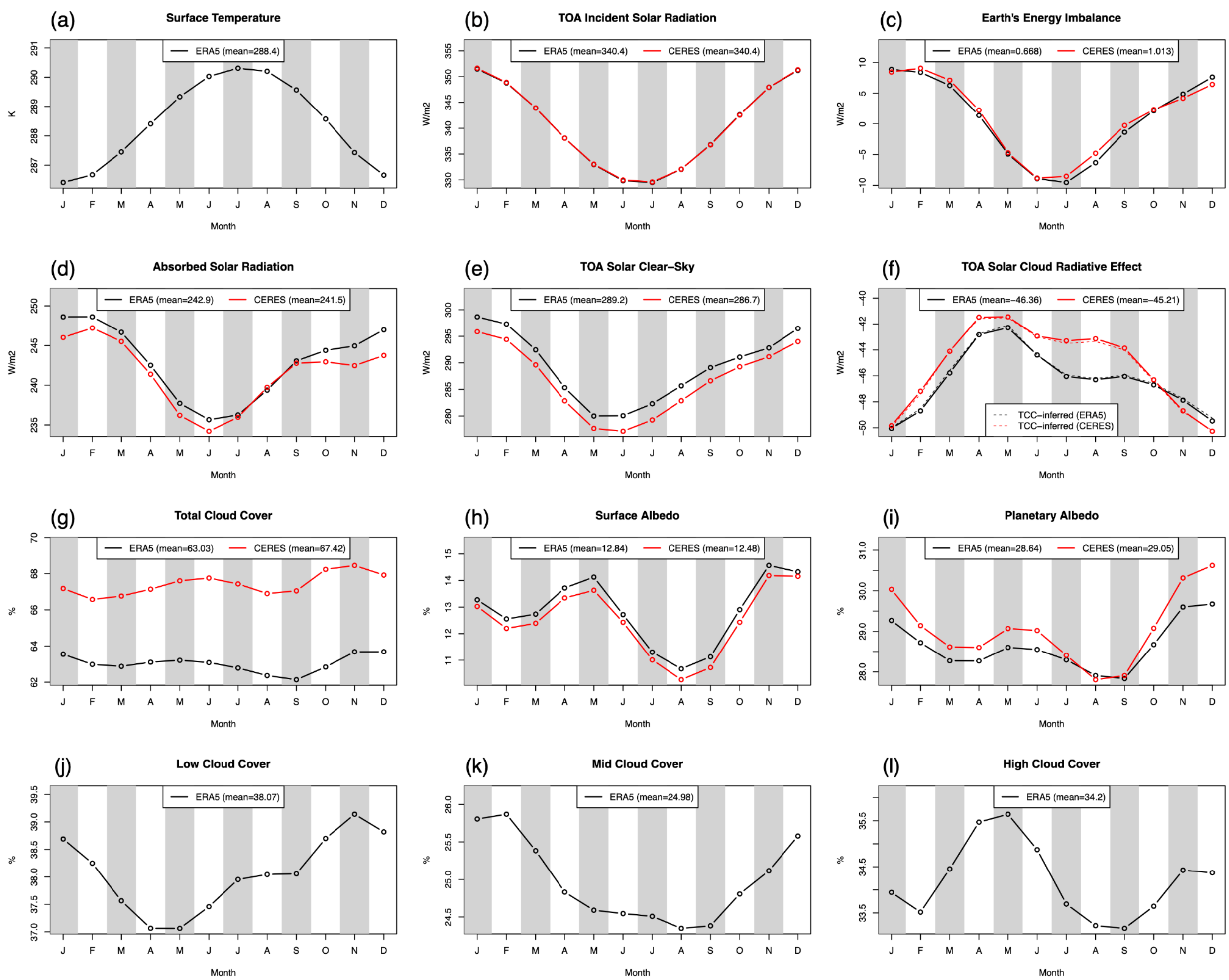

Fig. S1. Monthly climatologies of relevant quantities related to Earth's energy budget for 2001–2022. *(a) Surface (skin) temperature, (b) TOA incident solar radiation (ISR), (c) Earth's TOA total energy imbalance (EEI), (d) TOA net solar radiation (= absorbed solar radiation, ASR), (e) TOA net solar clear-sky radiation, (f) TOA net solar cloud radiative effect (CRE, solid) with values inferred from total cloud cover dashed (CREtc), (g) total cloud cover fraction, (h) surface albedo (derived from global-mean surface solar downwelling and upwelling radiation), (i) planetary albedo (derived from global-mean TOA incident solar and upwelling solar radiation), (j) mid-level cloud cover fraction, (k) mid-level cloud cover fraction, and (l) high-level cloud cover fraction. Red curves show CERES data and black curves show ERA5 data.*

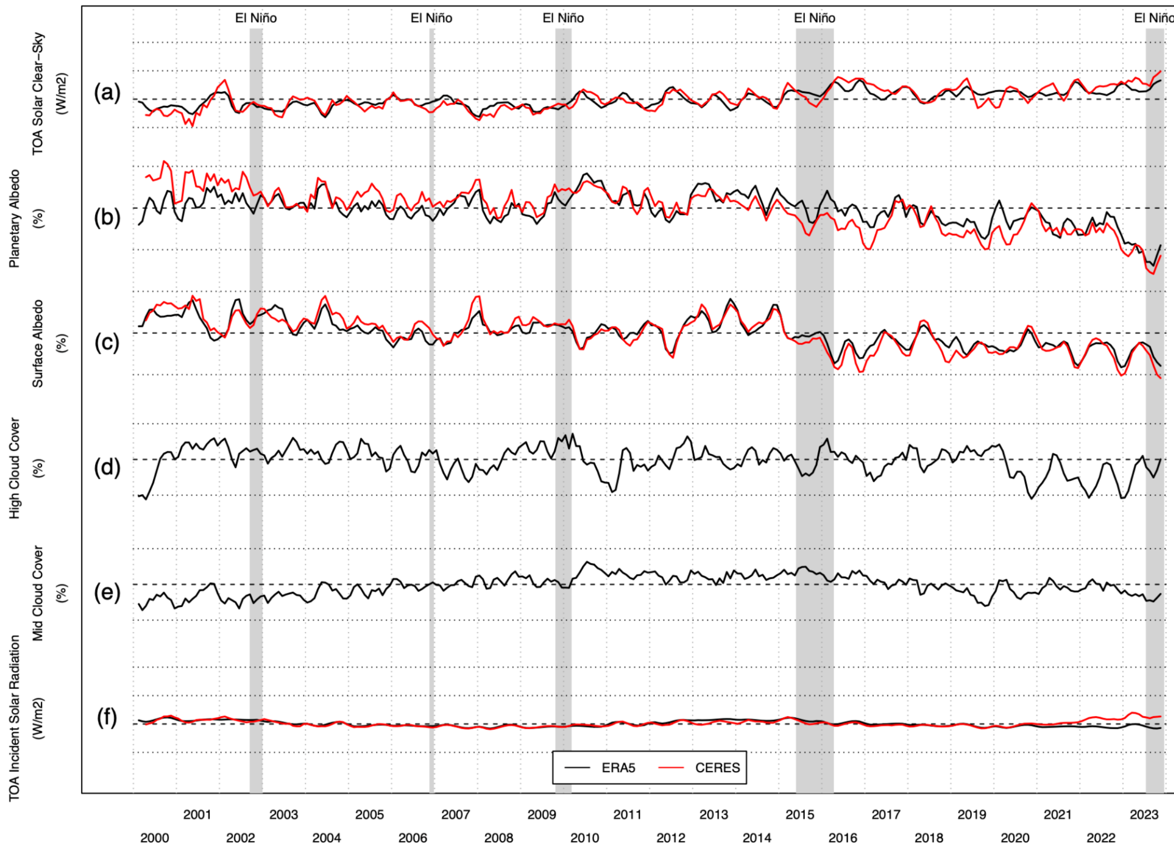

Fig. S2. Global-mean anomalies of additional quantities related to Earth's energy budget. *Three-monthly running-mean anomalies relative to 2001–2022 of (a) TOA net solar clear-sky radiation, (b) planetary albedo (derived from global-mean TOA incident solar and upwelling solar radiation), (c) surface albedo (derived from global-mean surface solar downwelling and upwelling radiation), (d) high-level cloud cover fraction, (e) mid-level cloud cover fraction, and (f) TOA incident solar radiation. Red curves show CERES data and black curves show ERA5 data. El Niño periods with anomalies exceeding +1K (see Fig.1b) are highlighted with gray shading.*

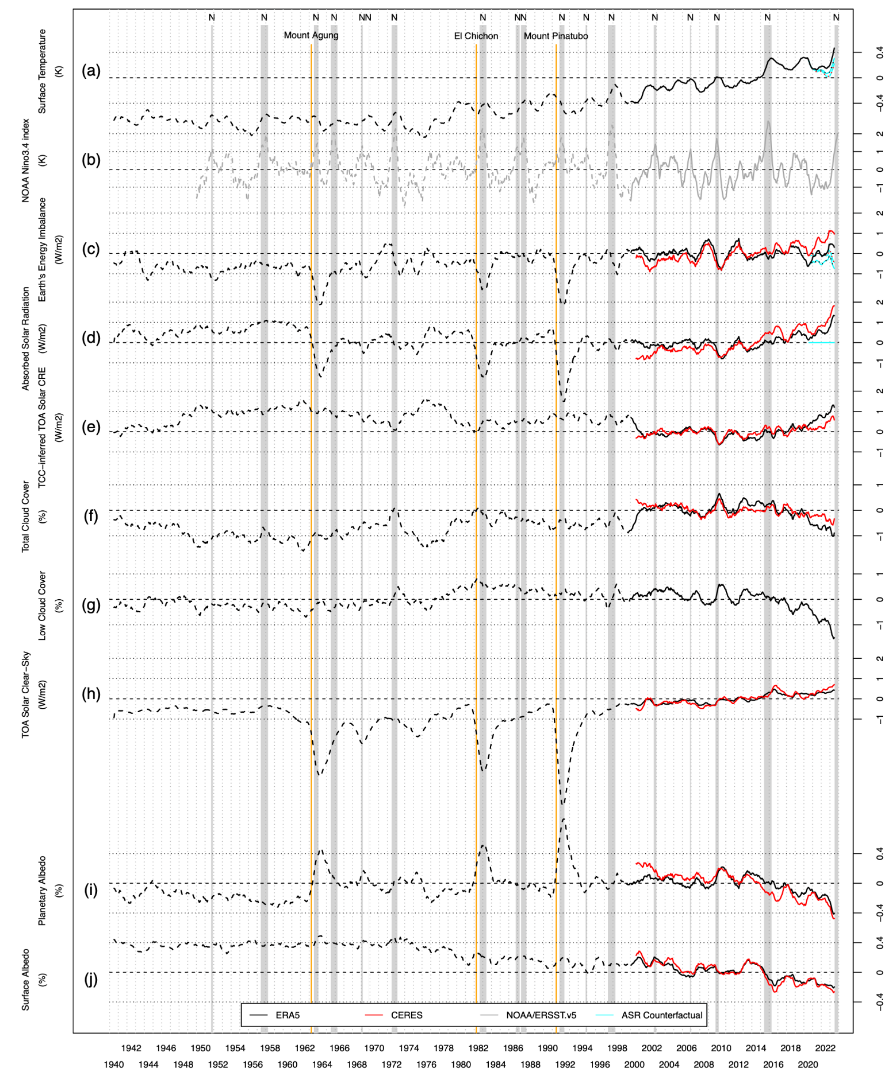

Fig. S3. Global-mean anomalies of selected quantities related to Earth's energy budget since 1940. *Twelve-monthly running-mean anomalies relative to 2001–2022 of (a) surface (skin) temperature, (b) NOAA Ocean Niño 3.4 index, (c) Earth's TOA total energy imbalance, (d) TOA net solar radiation (= absorbed solar radiation, ASR), (e) TOA solar cloud radiative effect inferred from total cloud cover anomalies, (f) total cloud cover fraction, (g) low-level cloud cover fraction, (h) TOA net solar clear-sky radiation, (i) planetary albedo (derived from global-mean TOA solar downwelling and upwelling radiation), and (j) surface albedo (derived from global-mean surface solar downwelling and upwelling radiation). Red curves show CERES data and black curves show ERA5 data. Cyan curves show counterfactuals based on a 2-layer energy balance model where ASR anomalies are assumed to be zero from the beginning of December 2020 onward. El Niño periods with anomalies exceeding +1K are highlighted with gray shading and labeled "N". Curves showing ERA5 data before 2000 are dashed to express that long-term trends can be spurious due to observing-system changes.*

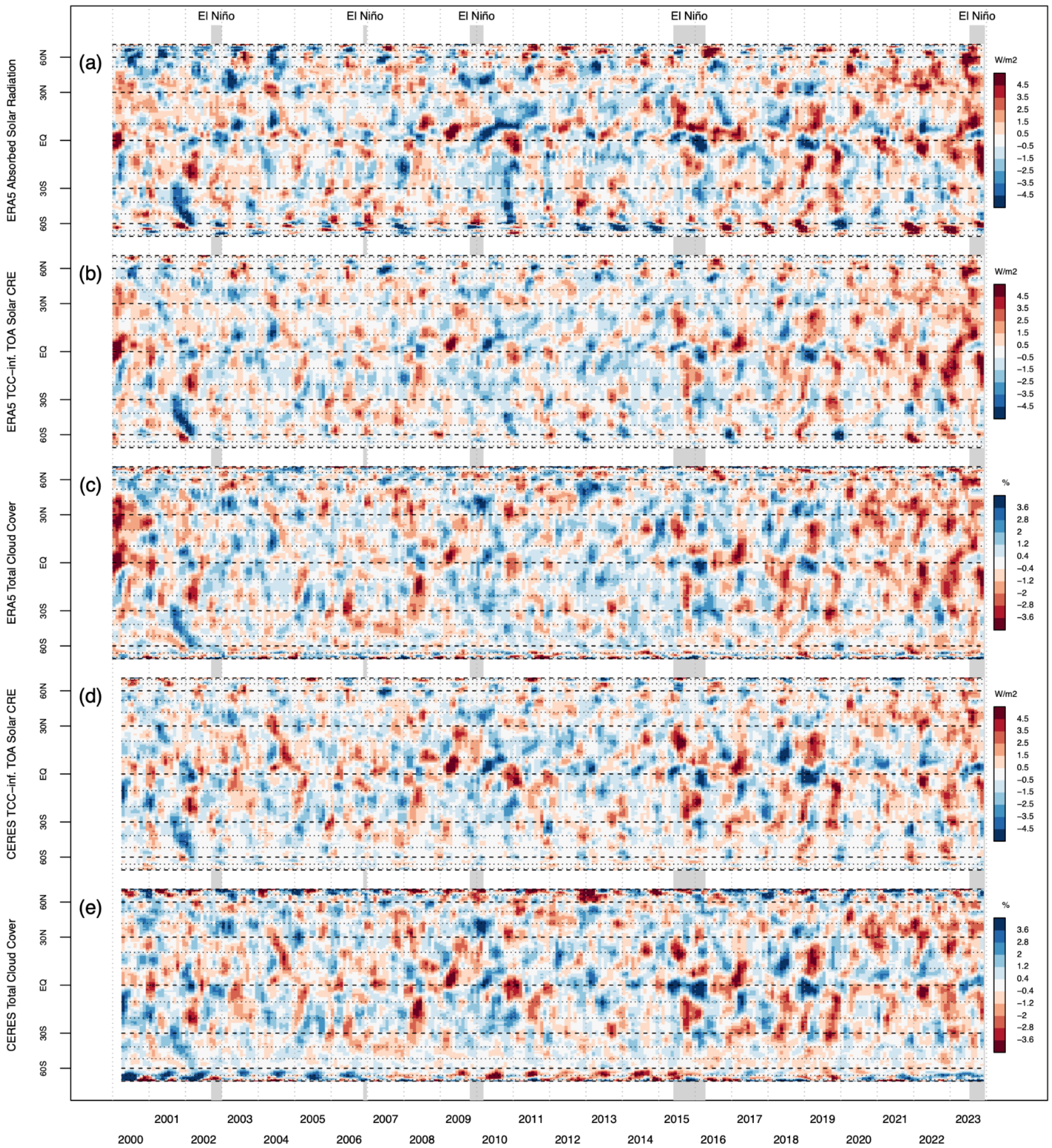

Fig. S4. Zonal-mean anomalies of additional quantities related to Earth's energy budget. *Three-monthly running-mean anomalies relative to 2001–2022 of (a) ERA5 absorbed solar radiation, (b) ERA5 cloud radiative effect inferred from total cloud cover anomalies, (c) ERA5 total cloud cover, (d) CERES TOA solar cloud radiative effect inferred from total cloud cover anomalies, and (e) CERES total cloud cover. El Niño periods with anomalies exceeding +1K are highlighted with gray shading. Latitude spacing corresponds to cosine(latitude) for an equal-area representation.*

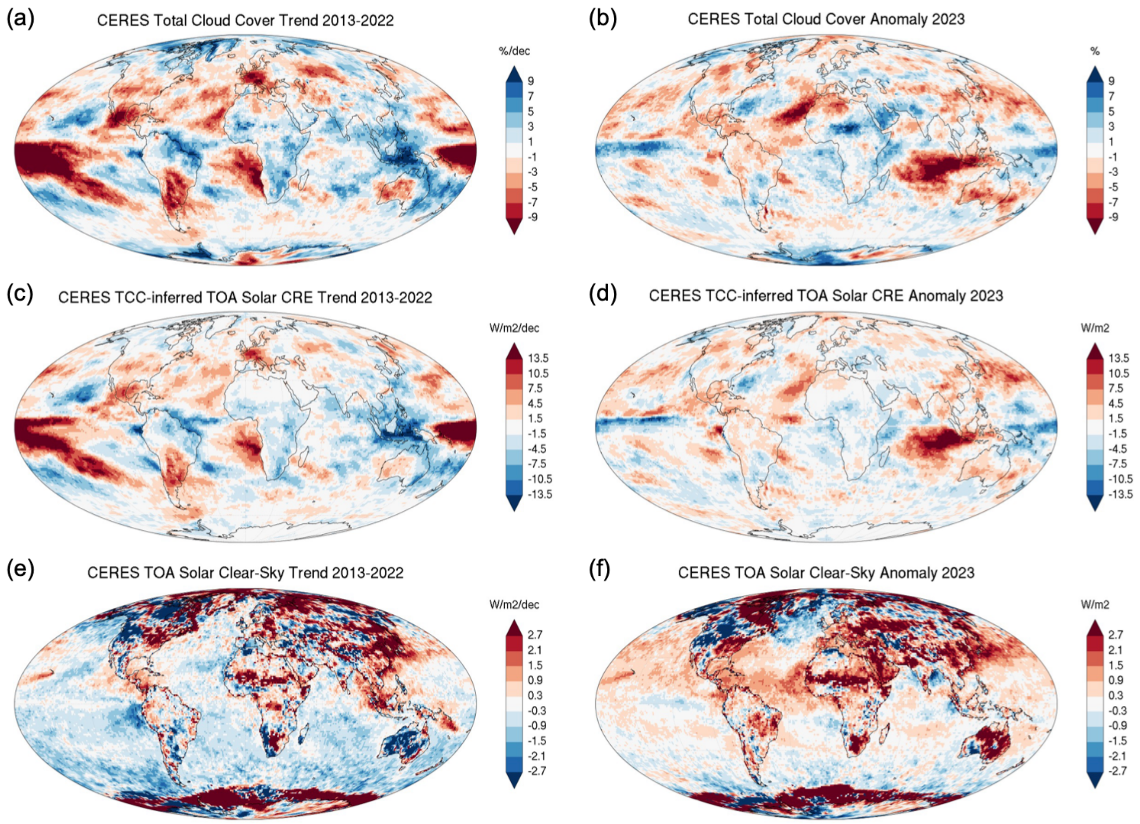

Fig. S5. Decadal 2013–2022 trends and annual-mean 2023 anomalies of additional parameters related to Earth's energy budget and clouds. *CERES trends and anomalies relative to 2001—2022 of (a,b) total cloud cover fraction, (c,d) TOA solar cloud radiative effect inferred from total cloud cover anomalies and (e,f) TOA net solar clear-sky radiation (color scale chosen to resolve anomalies over the open ocean).*

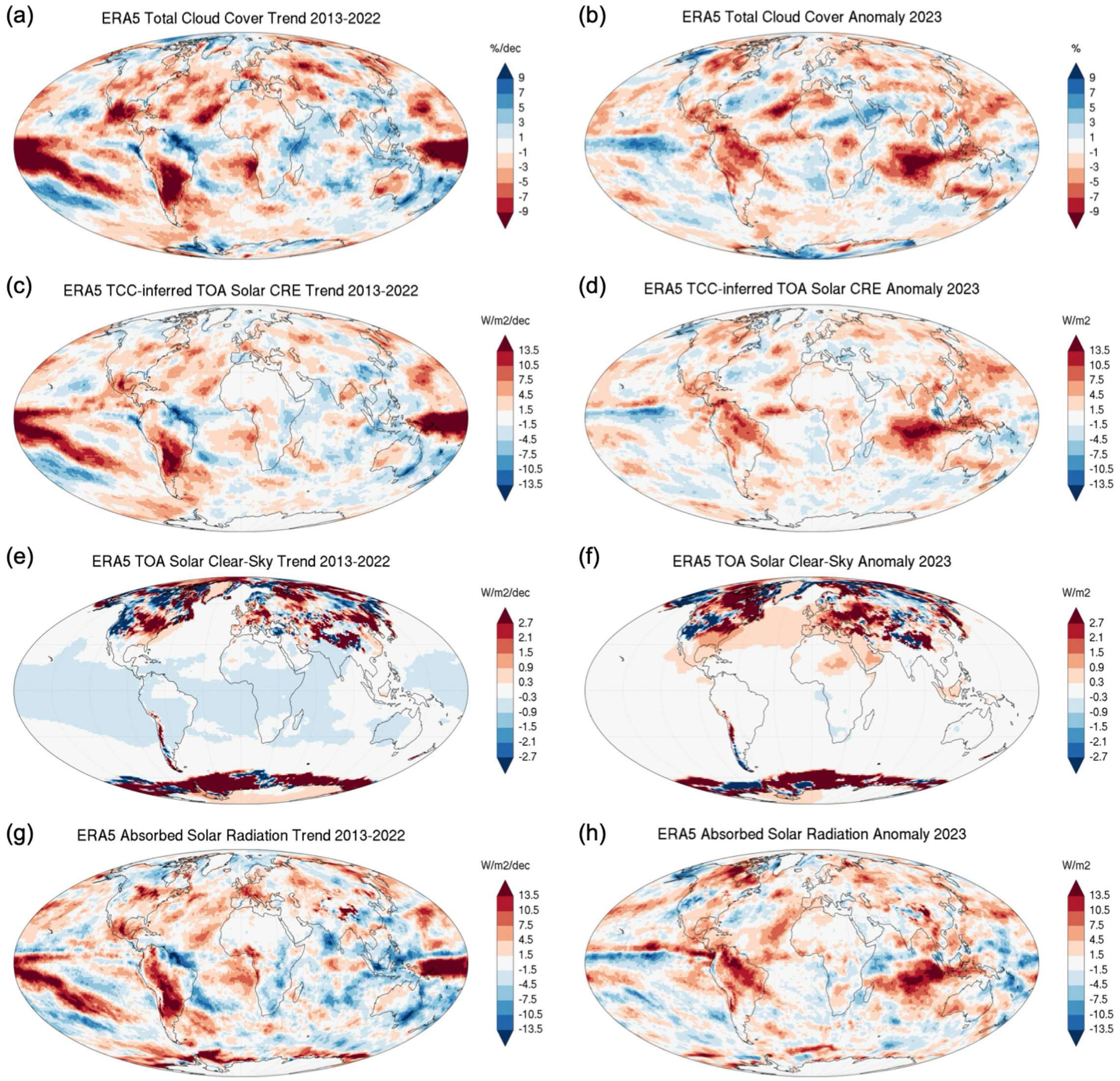

Fig. S6. Decadal 2013–2022 trends and annual-mean 2023 anomalies of additional parameters related to Earth's energy budget and clouds. *ERA5 trends and anomalies relative to 2001—2022 of (a,b) total cloud cover fraction, (c,d) TOA solar cloud radiative effect inferred from total cloud cover anomalies, (e,f) TOA net solar clear-sky radiation (color scale chosen to resolve anomalies over the open ocean) and (g,h) TOA net solar radiation (= absorbed solar radiation, ASR).*

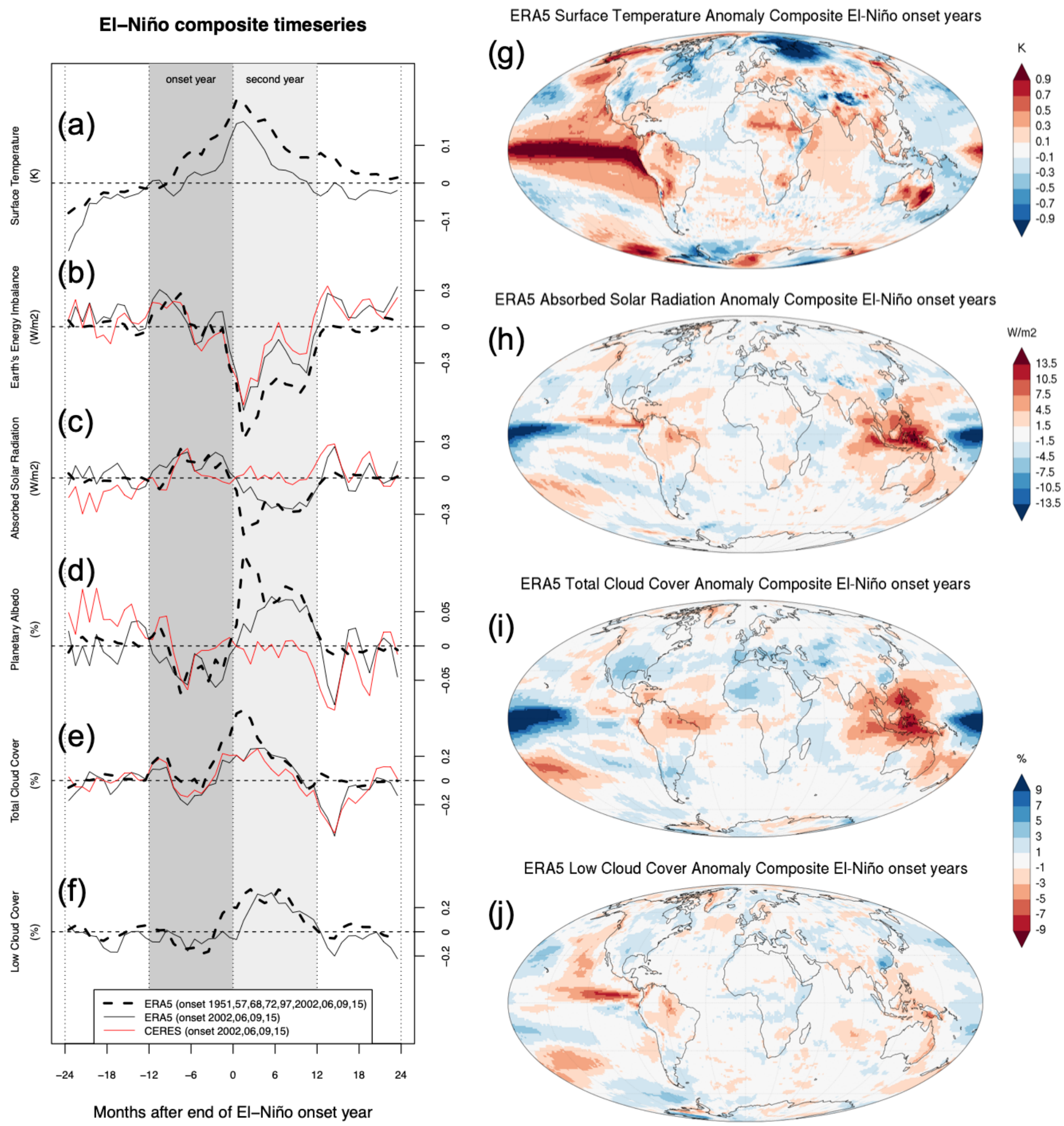

Fig. S7. El Niño composite analysis. *(a-f) Global-mean composites of 4 pre-2023 El Niño events covered by the CERES period based on CERES data (thin solid red curves) and ERA5 data (thin solid black curves) and of an extended set of 9 pre-2023 El Niño events based on ERA5 data (thick dashed black curves) for (a) surface (skin) temperature, (b) Earth's TOA total energy imbalance, (c) TOA net solar radiation (= absorbed solar radiation, ASR), (d) planetary albedo (derived from global-mean TOA solar downwelling and upwelling radiation), (e) total cloud cover fraction, and (f) low-level cloud cover fraction. (g-j) Annual-mean composites of 9 pre-2023 El Niño onset years based on ERA5 data (corresponding to the thick dashed black curves in a-f) for (g) surface (skin) temperature, (h) TOA net solar radiation (= absorbed solar radiation, ASR), (i) total cloud cover fraction, and (j) low-level cloud cover fraction.*

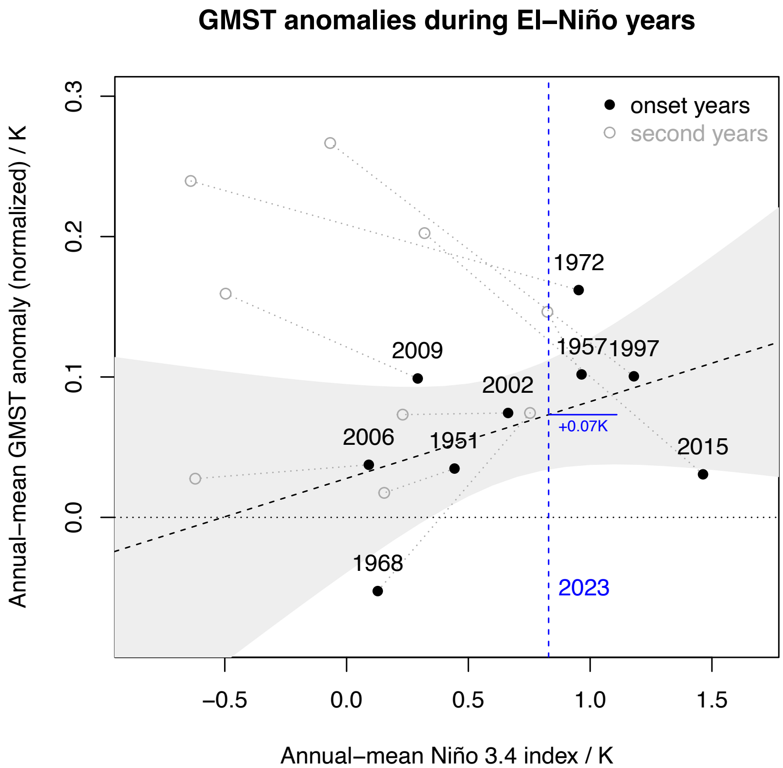

Fig. S8. Global-mean surface temperature anomalies during El Niño years. *Based on annual-means of NOAA Ocean Niño 3.4 index and ERA5 annual-mean surface (skin) temperature for 9 El Niño onset years (black filled circles) and corresponding second years (grey circles). The contribution of El Niño to the 2023 temperature anomaly (+0.07(±0.04)K) is estimated based on the 2023-mean Niño 3.4 index (blue dashed line) with linear least-square regression (black dashed line and 90% confidence band by gray shading).*

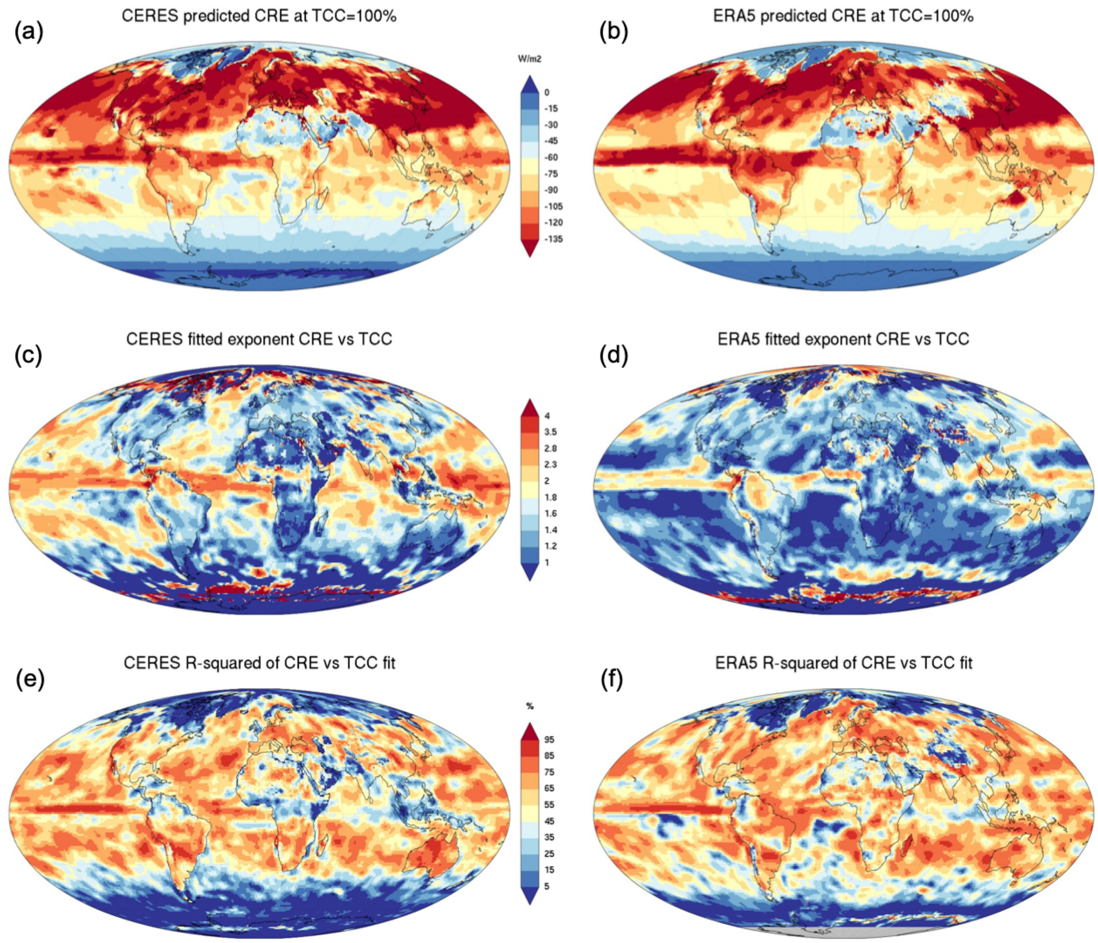

Fig. S9. Parameters of the power functions fitted to the TCC-CRE-relation for May. *Based on inter-annual variations of monthly data 2001–2014, with May chosen arbitrarily as an example. (a) linear coefficient α corresponding to the predicted CRE at TCC=100% based on CERES; (b) same but based on ERA5; (c) exponent β with values above 1 indicating a superlinear dependence of CRE on TCC based on CERES; (d) same but based on ERA5; (e) Fraction of CRE variance explained by the fit based on CERES; (f) same but based on ERA5.*

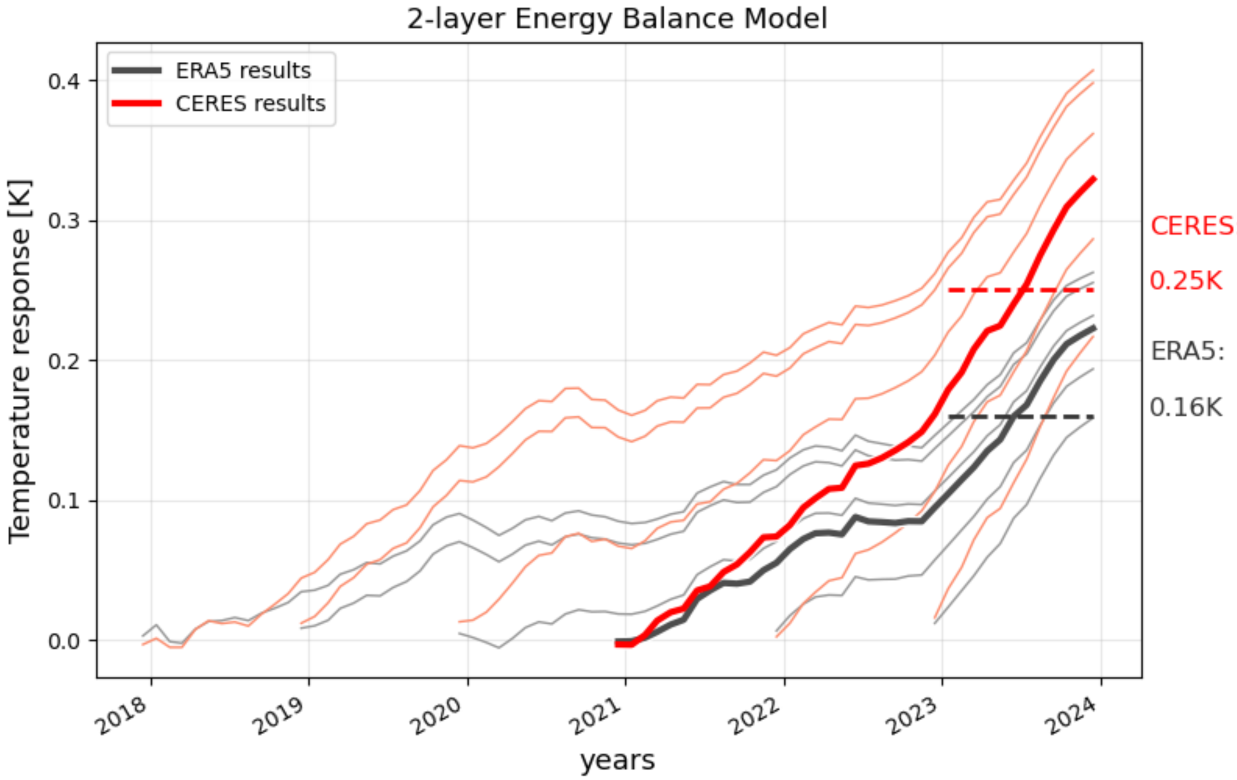

Fig. S10. Upper-layer temperature response [K] to anomalous absorbed solar radiation from the CERES (red lines) and ERA5 (gray lines) datasets with respect to their 2001-2022 climatology. *The temperature estimate is computed with the 2-layer Energy Balance Model. Individual lines are initialized from December 2017 until December 2023, and then the solution to the EBM is found until December 2023. Horizontal dashed lines give the mean temperature response for the whole year 2023 (CERES: 0.25K, in red; ERA5: 0.16K, in black) for solutions initialized in December 2020, respectively.*

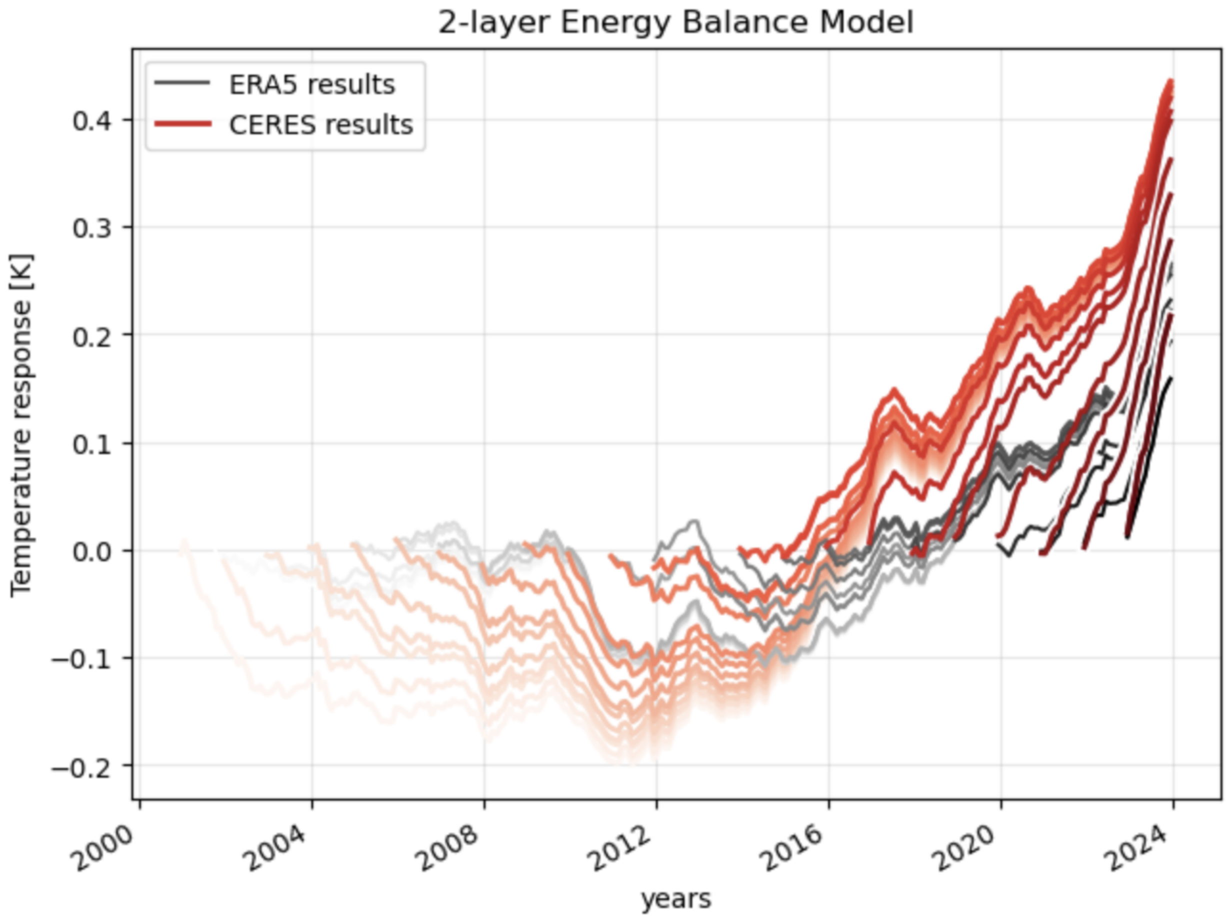

Fig. S11. Upper-layer temperature response [K] to anomalous absorbed solar radiation from the CERES (red lines) and ERA5 (gray lines) datasets with respect to their 2001-2022 climatology. *The temperature estimate is computed with the 2-layer Energy Balance Model. Individual lines are initialized from all Decembers in the period December 2000 to December 2023, and then the solution to the EBM is found until December 2023.*

Table S1.

Parameters used in the 2-layer Energy Balance Model in this study. The parameters follow (42) and (44). By excluding the INM-CM4 model, the fitted ensemble-mean deep-ocean heat capacity $\boldsymbol{C_0}$ *has a much smaller standard deviation of 27 W yr m*$^{-2}$ *K*$^{-1}$ *(44), indicating that the INM-CM4 might be an outlier in the multi-model CMIP ensemble, and therefore the parameters based on the remaining models are used here.*

F_{eff} (forcing efficacy)	**λ (radiative feedback parameter)**	**γ (heat exchange coefficient)**	**$\boldsymbol{C}$ (upper heat capacity)**	**$\boldsymbol{C_0}$ (deep-ocean heat capacity)**
0.92 (*ref 42*)	1.13 W m^{-2} K^{-1} (MMM in Table 3 in *ref 44*)	0.74 W m^{-2} K^{-1} (MMM in Table 4 in *ref 44*)	7.3 W yr m^{-2} K^{-1} (MMM in Table 4 in *ref 44*)	91.0 W yr m^{-2} K^{-1} (MMM in Table 4 in *ref 44*)